



# Comparative Study of Skin–Stringer Connection Approaches for Stiffened Structures with Curvilinear Stiffeners

Wei Zhao\*

Oklahoma State University, Stillwater, Oklahoma 74078

and

Junhyeon Seo<sup>†</sup> and Rakesh K. Kapania<sup>‡</sup>

Virginia Polytechnic Institute and State University, Blacksburg, Virginia 24061

<https://doi.org/10.2514/1.J062923>

Additive manufacturing enables the deposition of material in the near-net shape at any desired location on the base plate or shell to improve the structural performance by tailoring the buckling and/or vibration mode shapes. In this study, a stiffened plate with arbitrarily shaped stiffeners is modeled using a nonconformal mesh-based finite element model. Six degrees of freedom are considered for each node of the plate and the stiffener finite element models to enable the couplings between the plate's and stiffeners' in-plane and out-of-plane motions. Displacement compatibility is enforced at the interface between the plate and the stiffeners where several skin–stringer connection approaches, including inverse isoparametric mapping algorithm (IIMA), radial basis function, and thin-plate spline function, are used. Various complex models available in the literature are employed for evaluating the skin–stringer connection approaches. Research studies show that the IIMA-based nonconformal mesh modeling can generate a sparse displacement approximation matrix, which makes it an efficient approach for nonconformal mesh-based modeling. For the stiffened plate with higher stiffeners, the present results agree well with those obtained from the Abaqus/CAE conventional conformal mesh and mesh tie constraint-based nonconformal mesh modeling results, but yield better results than the Abaqus/CAE wrapping mesh approach.

## Nomenclature

$A$	= relation matrix between leader degree of freedom and follower degree of freedom
$a$	= coefficients for radial basis functions used in stiffener nodal displacement interpolation functions
$B$	= strain–displacement matrix
$b_s$	= width of blade-stiffener cross section, m
$D$	= constitutive matrix giving stress resultant–strain relations
$d$	= unknown nodal displacement vector
$d_p$	= plate nodal displacement vector
$d_s$	= stiffener element nodal displacement vector described in a local coordinate system
$d_{sg}$	= stiffener element nodal displacement vector described in a global coordinate system
$E$	= Young's modulus, Pa
$e$	= eccentricity of stiffener, $(1/2)(t_p + h_s)$ , m
$F$	= applied external load, N
$G$	= shear modulus, Pa
$H_{sp}$	= interpolation matrix to approximate each degree-of-freedom vector for the stiffener nodal displacements
$h_s$	= height of blade-stiffener cross section, m
$J$	= Jacobian of coordinate transformation
$K_{Gp}$	= panel geometric stiffness matrix
$K_{Gs}$	= stiffener geometric stiffness matrix

$K_p$	= panel elastic stiffness matrix
$K_s$	= stiffener elastic stiffness matrix
$m$	= number of stiffener element nodes
$N_{sp}$	= interpolation matrix to approximate stiffener nodal displacements
$n$	= number of plate element nodes
$p$	= low-order polynomials used in stiffener nodal displacement approximation
$Q$	= stress–strain relation
$r$	= geometry field for a point, $(x, y, z)$
$T_p$	= selection matrix used in multiquadric radial basis function
$T_s$	= coordinate transformation matrix for stiffener nodal displacements
$t, n, b$	= curvilinear stiffener tangential, normal, and binormal directions, respectively
$t_p$	= panel thickness, m
$u_p$	= each degree-of-freedom vector in panel nodal displacement vector
$u_s$	= each degree-of-freedom vector in stiffener nodal displacement vector
$\alpha$	= coefficients for low-order polynomial used in stiffener nodal displacement interpolation functions
$\Gamma$	= stiffener arc length domain
$\Delta d$	= initial nodal displacement vector
$\epsilon, \sigma$	= strain and stress, Pa, respectively
$\lambda_b$	= buckling load factor
$\sigma^0$	= external in-plane stress, Pa
$\sigma_p$	= stress-resultant matrices for plate and stiffeners, respectively, N/m
$\sigma_s$	= matrix for radial basis functions
$\phi$	= radial basis function
$\Psi_p$	= panel buckling mode shape vector
$\Omega$	= panel area domain

## Subscripts

$p$	= plate
$s$	= stiffener
$t$	= total model (i.e., stiffened plate)

Presented as Paper 2023-1522 at the SciTech 2023, National Harbor, MD and Online, January 23–27, 2023; received 19 February 2023; revision received 18 May 2023; accepted for publication 21 May 2023; published online 21 July 2023. Copyright © 2023 by Wei Zhao, Junhyeon Seo, and Rakesh K. Kapania. Published by the American Institute of Aeronautics and Astronautics, Inc., with permission. All requests for copying and permission to reprint should be submitted to CCC at www.copyright.com; employ the eISSN 1533-385X to initiate your request. See also AIAA Rights and Permissions www.aiaa.org/randp.

\*Assistant Professor, School of Mechanical and Aerospace Engineering; wzhao@okstate.edu. Senior Member AIAA.

<sup>†</sup>Postdoctoral Research Associate, Department of Mechanical Engineering. Member AIAA.

<sup>‡</sup>Mitchell Professor, Kevin T. Crofton Department of Aerospace and Ocean Engineering. Fellow AIAA.

*Superscripts*

$e$	= element property
NL	= nonlinear term

**I. Introduction**

**A**DITIVE manufacturing (AM) technologies enable the light-weight airplane wingbox design through fabricating complex shape structures close to the designs found in nature with least waste of the raw material (see the two stiffened plate models fabricated using traditional machining and AM [1,2], as shown in Fig. 1). In addition to optimizing the geometric properties of the stiffeners to improve the structural buckling performance [3], recent studies on design optimization of aircraft panels using curvilinear stiffeners revealed that it is possible to tailor the stiffener's shape to improve both the buckling and vibration responses of stiffened structures [4–9]. Many efforts have been made toward performing structural analysis and design optimization of curvilinearly stiffened plates. Kapania et al. [4] developed an optimization framework by using commercial software, MSC PATRAN/NASTRAN, for design optimization of curvilinearly stiffened plates. Dang et al. [10] used Abaqus/CAE to conduct a stiffener layout design for a plate with two cutouts. Mulani et al. [6] developed an improved optimization framework for studying both curvilinearly stiffened flat and curved panels subject to complex loads and boundary conditions.

A challenging task in these optimization frameworks [4,6,10] was to develop a conformal mesh-based finite element model (FEM) for the curvilinearly stiffened structure when the stiffener shape is very complex. For the conformal mesh-based FEMs, the nodes for stiffeners and plate should coincide at plate-stiffener and stiffener-stiffener interfaces. However, meshing often fails when satisfying such element nodal coincidences, especially when the number of stiffeners becomes large or the stiffeners' geometric shapes become very complex. A fine mesh was often used to avoid excessive meshing failure at the price of an expensive structural analysis [6].

To overcome the meshing issues faced in the conformal mesh-based FEMs for structure analysis and optimization of stiffened plates with any shape and any number of stiffeners, there are some developed nonconformal meshing techniques available in the commercialized finite element analysis software: glued contact [11], available in MSC PATRAN/NASTRAN, and tie contact, available in Abaqus/CAE [12]. These nonconformal meshing techniques use multipoint constraints (MPCs) to connect two surfaces together when the plate and the stiffeners have dissimilar mesh at their interfaces. The glued and tied contact use MPCs, also called multifreedom constraints by Felippa [13], which is a method when different nodes and degrees of freedom (DOF) are connected together, in a leader-and-follower behavior. There are three common methods based on their relations used in the glued/tied contact-based nonconformal mesh modeling: 1) follower DOF elimination method, 2) penalty

method, and 3) Lagrange multiplier method. The details about these approaches can be found in Ref. [13]. Singh et al. [9] employed the glued contact for studying the buckling load maximization of curvilinearly stiffened shells. The finite element nodes on the shell-stiffener interfaces during meshing are not required to coincide, as often seen in the conformal mesh modeling. Nevertheless, the conformal mesh is still considered for the stiffeners, where the finite element nodes coincide at the stiffener-stiffener intersections while employing NASTRAN glued contact and Abaqus/CAE tie contact. There is another nonconformal meshing technique, namely, wrap mesh approach (WMA) [14], available in Abaqus/CAE, where there is no need to use conformal mesh for the stiffeners and plate. Alhajahmad and Mittelstedt [15] used this approach to study buckling of grid-stiffened composite structures, where the stiffeners and plate connect in the form of surface-to-surface contact. The stiffeners were modeled as shell elements, but they were meshed in the plane parallel to the plate median plane. The stiffener height was treated as the shell thickness for the stiffener elements.

In addition to using a rigid-body motion relation for all leader and follower nodes DOF, an inverse isoparametric mapping algorithm (IIMA) [16] has been employed to enable the skin-stringer connections for the nonconformal mesh modeling of curvilinearly stiffened plates [7,8,17–20]. The IIMA is a locally supported interpolation function, as it uses a piecewise shape function for the isoparametric plate element where the stiffener node is located. Based on the isoparametric shape function used in the finite element method, each stiffener nodal displacement can be approximated using the nodal displacements for each plate element. The stiffener's stiffness matrix can be transformed to those for the plate. Nevertheless, the challenge of using the IIMA is to compute the natural coordinates for the isoparametric plate-element shape function to approximate the displacement for each stiffener element node. A globally supported radial basis function (RBF) was later considered by Zhao and Kapania [21] to approximate each stiffener nodal displacement by using all plate-element nodal displacements. A compactly supported RBF using  $C^2$  Wendland basis function was employed. However, in the  $C^2$  Wendland basis function-based RBF, one needs to choose a proper support radius as used in the stiffener displacement approximation. Research studies show that the support radius is model dependent, which should be selected in a proper way to avoid inaccurate structural analysis results [21,22]. Wei et al. [22] suggested using 2.2 times the mesh size of the plate for determining the support radius when a uniform mesh is considered for a plate model. There is a potential challenge in selecting a proper support radius for plates with nonuniform mesh. For the plates with multicutouts, a nonuniform mesh size is often used; it is not convenient to determine a proper support radius for the  $C^2$  Wendland function-based RBF. Therefore, in this study, we also investigate other widely used interpolation functions, including thin-plate spline (TPS) function and other basis functions for the RBF.

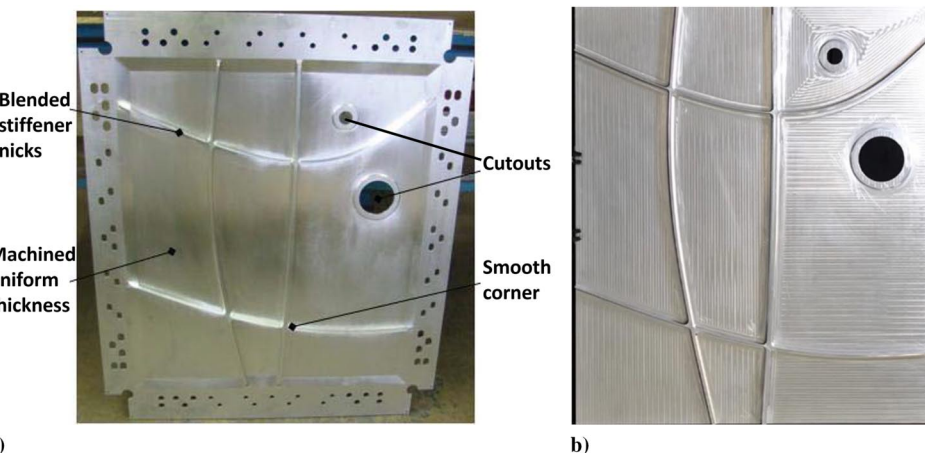


**Fig. 1** Curvilinearly stiffened structures fabricated using a) traditional machining from a plate stock [1] and b) additive friction stir deposition [2]. (Reprinted in part with permission from Nanci Hardwick of MELD Manufacturing Corp.)

The mesh-free and isogeometric methods were also developed for studying the structural responses of the stiffened plate with arbitrarily shaped stiffeners. Tamjani and Kapania [23,24] studied the static, buckling, and vibration responses of curvilinearly stiffened plates using mesh-free method. Moving-least-squares approximation is used to construct the shape functions. The parameters for the stiffener displacement are approximated using those for the plate through the displacement compatibility at the plate–stiffener interface. Qin et al. [25] used an isogeometric method to study static and dynamic responses of a stiffened plate with arbitrarily shaped stiffeners. The geometry and displacement for the control points of the stiffener element can be approximated by those of the plate element where the control points of the beam element are located. This method was also employed by Saeedi et al. in their work [26]. Hao et al. [27] used an isogeometric method for studying static and buckling analyses of a stiffened plate and shell structures with arbitrarily shaped stiffeners, where a nonuniform rational B-spline (NURBS)-based three-dimensional (3-D) degenerated beam element was used for modeling the stiffeners. To enable the displacement compatibility between the stiffeners and the base structures, they used simple matching of NURBS control points for flat plate and an improved point-to-surface projection algorithm for complex shape geometry base structures.

For grid-stiffened plates with straight or curved grid stiffeners, homogenization approaches have been widely used for an efficient structural analysis. Jaunay et al. [28] used a smeared stiffener theory for buckling analysis of grid-stiffened composite panels, where the skin–stiffener coupling was considered. Wodesenbet et al. [29] developed an improved smeared method for an isogrid stiffened composite cylinder, where the stiffeners are computed by analyzing the force and moment effect of the stiffener on a unit cell. Nemeth [30] developed an equivalent plate continuum stiffness for eccentrically stiffened plates based on the first-order transverse shear deformation plate theory for three representative isogrid stiffeners. Chen et al. [31] used a variational asymptotic homogenization method for structural analysis of isogrid stiffened structures. Wang et al. [32] used a novel numerical implementation of asymptotic homogenization-based smeared stiffener method to study the global buckling of grid-stiffened composite cylindrical shells. Liu et al. [33] used a structure genome-based homogenization approach for studying the global buckling of composite stiffened plates. Wang and Abdalla [34] developed a smeared stiffener approach based on the conservation of the strain energy for various grid-stiffened plates. The homogenization-based global/local analysis is used to calculate structural responses on a global unstiffened model with the equivalent material properties obtained from local representative cell configurations. However, as mentioned by Wang et al. [35], the homogenization approach is intended for densely distributed stiffeners, whose shape behaves in a periodic variation across the plate and shell structures. When the stiffeners are sparsely distributed, the performances evaluated using homogenization may not be accurate. The present paper focuses on studying buckling of stiffened structure with any number and any shape of stiffeners. The presented approaches enable a fast yet accurate buckling mode result prediction for the structure with different stiffener designs. The remaining part of this

paper is organized as follows. Section II briefly presents the finite element method for performing buckling analysis of stiffened plates by using nonconformal mesh modeling approaches for the curvilinearly stiffened structures. Section III presents the stiffener displacement approximation in terms of the plate displacements by using IIMA, RBFs using  $C^2$  Wendland function and multiquadric (MQ) function, and TPS functions. Section IV presents buckling results of a complex curvilinearly stiffened tow-steered laminated plate using different skin–stringer connection approaches. All methods are used to study the buckling responses of a rectangular stiffened plate with multicuts in Sec. V. Section VI presents the buckling results studied using the present nonconformal mesh with the most efficient IIMA skin–stringer connection approach and Abaqus/CAE conformal and WMA nonconformal mesh-based finite element models. The last section, Sec. VII, concludes the present work.

## II. Finite Element Buckling Analysis

The stiffeners are mainly used to increase the local stiffness of the plate to increase the structure bending stiffness or to modify the buckling and/or vibration mode shapes to improve the structural stability and dynamic response. Here, only the buckling response of a plate with arbitrarily shaped stiffeners is investigated. Consider a curvilinearly stiffened plate, as shown in Fig. 2. In this study, the plate is modeled as two-dimensional (2-D) shell elements, and each stiffener is modeled as a 3-D beam. For a stiffened plate with eccentric stiffeners, in addition to the in-plane and out-of-plane motion coupling, there is also a coupling between the in-plane drilling rotational angle and the in-plane axial displacement of the stiffener. Therefore, we improve previous modeling approaches on stiffened plates [7] by considering six DOF for each node of the FEM. The generalized stress resultants and strain relations for the plate and stiffeners are presented in Appendices A and B, respectively.

In the design of thin-walled stiffened structures, an individual stiffener buckling is not expected in the stiffened plate designs. Moreover, studies by Mittelstedt [36] and Zhao and Kapania [7] have shown that further increasing the stiffener height only causes a slight increase in the buckling load, while the buckling load efficiency, which refers to the ratio of the buckling load over the total weight, reduces with the stiffener height. A buckling analysis example studied by Stanford et al. and Townsend and Kim [37,38] for saving space, presented in Appendix C has shown that the buckling load efficiency will reduce with the stiffener depth ratio when a much deeper stiffener is used. The beam-based stiffener modeling for the stiffened plate can accurately predict the buckling loads of the stiffened plate with deep stiffeners. Therefore, in the present study, to address the challenge of using stiffener with arbitrary shapes and layouts in the design process, we consider modeling stiffeners as beam elements for an efficient buckling analysis and design of stiffened plates. For buckling analysis of the stiffened plate, there are normally two steps considered: pre-buckling static analysis and eigenvalue-based buckling analysis. Both displacement control and load control are considered for the examples studied in this paper.

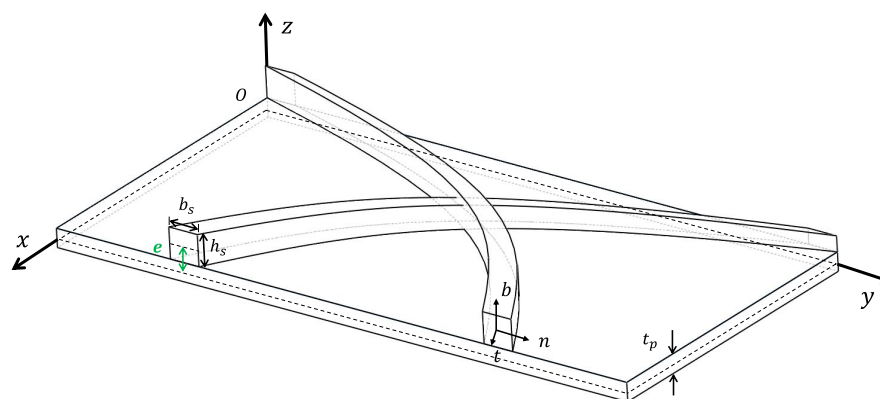


Fig. 2 Schematic of a curvilinearly stiffened plate [21].

## A. Pre-Buckling Static Analysis

### 1. Displacement Control

For a stiffened plate subjected to an in-plane axial end shortening,  $\Delta d$ , a static analysis is conducted as

$$[\mathbf{K}]\{\mathbf{d}_p\} = \begin{bmatrix} (\mathbf{K}_{11})_{k \times k} & (\mathbf{K}_{12})_{k \times l} \\ (\mathbf{K}_{21})_{l \times k} & (\mathbf{K}_{22})_{l \times l} \end{bmatrix} \begin{Bmatrix} \Delta \mathbf{d} \\ \mathbf{d} \end{Bmatrix} = \begin{Bmatrix} \mathbf{f} \\ \mathbf{0} \end{Bmatrix} \quad (1)$$

where  $k$  is the number of DOF with known displacements, including enforced boundary conditions, and  $l$  is the number of unknown displacements. The total stiffness matrix,  $\mathbf{K} = \mathbf{K}_p + \mathbf{K}_s$ , where  $\mathbf{K}_p$  is the plate's elastic stiffness matrix and  $\mathbf{K}_s$  is the stiffener's elastic stiffness matrix transformed to those for the plate model. The element stiffness matrices for  $\mathbf{K}_p$  and  $\mathbf{K}_s$  are given in Eq. (2):

$$\mathbf{K}_p^e = \int_{-1}^{+1} \int_{-1}^{+1} \mathbf{B}_p^T \mathbf{D}_p^T \mathbf{B}_p \det \mathbf{J}_p d\xi d\eta \quad (2a)$$

$$\mathbf{K}_s^e = (\mathbf{N}_{sp}^e)^T \left( \int_{-1}^{+1} \mathbf{T}_s^T \mathbf{B}_s^T \mathbf{D}_s^T \mathbf{B}_s \mathbf{T}_s \det \mathbf{J}_s d\xi \right) \mathbf{N}_{sp}^e \quad (2b)$$

The matrices given in Eq. (2) can be found in our previous work [7]. Matrix  $\mathbf{N}_{sp}$  is the stiffener nodal displacement interpolation matrix, which will be calculated using different approaches, as presented in Sec. III.

Based on Eq. (1), the unknown displacement  $\mathbf{d}$  can be computed using the following equation:

$$\mathbf{K}_{22}\mathbf{d} = -\mathbf{K}_{21}\Delta\mathbf{d} \quad (3)$$

Finally, the nodal displacement vector for the plate is summarized as

$$\{\mathbf{d}_p\} = \begin{Bmatrix} \Delta \mathbf{d} \\ \mathbf{d} \end{Bmatrix} \quad (4)$$

### 2. Load Control

For the stiffened plate subjected to an external load,  $\mathbf{F}$ , a static analysis is conducted using the following equation:

$$[\mathbf{K}_p + \mathbf{K}_s]\{\mathbf{d}_p\} = \mathbf{F} \quad (5)$$

The nodal displacement vector for the plate can be easily obtained through the preceding equation after enforcing the required boundary conditions.

### 3. Stress Recovery

The in-plane stresses for both the plate and the stiffeners on the reference plane are solved by using the following equations:

$$\boldsymbol{\sigma}_p^0 = \mathbf{Q}_p \boldsymbol{\epsilon}_p = \mathbf{Q}_p \mathbf{B}_p \mathbf{d}_p \quad (6a)$$

$$\boldsymbol{\sigma}_s^0 = \mathbf{Q}_s \boldsymbol{\epsilon}_s = \mathbf{Q}_s \mathbf{B}_s \mathbf{T}_s \mathbf{N}_{sp} \mathbf{d}_p \quad (6b)$$

where the strains  $\boldsymbol{\epsilon}_p$  and  $\boldsymbol{\epsilon}_s$  have different values when they are computed at different Gauss integration points. Averaged strains for the plate and the stiffeners are used to compute the in-plane stresses and geometric stiffness matrices. All of these matrices can be found in our previous work [39].

## B. Buckling Analysis

The buckling load factor  $\lambda_b$  can be obtained through an eigenvalue analysis:

$$[(\mathbf{K}_p + \mathbf{K}_s) + \lambda_b(\mathbf{K}_{Gp} + \mathbf{K}_{Gs})]\{\Psi_p\} = \mathbf{0} \quad (7)$$

where  $\Psi_p$  is the plate's buckling mode shape;  $\mathbf{K}_{Gp}$  and  $\mathbf{K}_{Gs}$  are the geometric stiffness matrices for the plate and the stiffeners,

respectively. The element geometric stiffness matrices,  $\mathbf{K}_{Gp}^e$  and  $\mathbf{K}_{Gs}^e$ , respectively, are

$$\mathbf{K}_{Gp}^e = \int_{-1}^{+1} \int_{-1}^{+1} (\mathbf{B}_p^{\text{NL}})^T [\boldsymbol{\sigma}_p] \mathbf{B}_p^{\text{NL}} \det \mathbf{J}_p d\xi d\eta \quad (8a)$$

$$\mathbf{K}_{Gs}^e = (\mathbf{N}_{sp}^e)^T \left( \int_{-1}^{+1} \mathbf{T}_s^T (\mathbf{B}_s^{\text{NL}})^T [\boldsymbol{\sigma}_s] \mathbf{B}_s^{\text{NL}} \mathbf{T}_s \det \mathbf{J}_s d\xi \right) \mathbf{N}_{sp}^e \quad (8b)$$

The matrices  $\mathbf{J}_p$  and  $\mathbf{J}_s$  are the Jacobians for the plate and the stiffeners, respectively;  $[\boldsymbol{\sigma}_p]$  and  $[\boldsymbol{\sigma}_s]$  are stress-resultant matrices for the plate and the stiffeners, respectively, based on the recovered stress for the plate and the stiffeners computed using Eq. (6), whose complete expressions are given in Ref. [7]. Gauss quadrature is used for numerical integration to obtain these elemental stiffness matrices [40].

## III. Skin–Stringer Connection Approaches

The stiffener nodal displacement approximation matrix  $\mathbf{N}_{sp}$  shown in Eqs. (2) and (8) is obtained using various skin–stringer connection approaches. This section explains four different skin–stringer connection approaches, as studied in the present work, including IIMA, RBF using  $C^2$  Wendland function and MQ function, and TPS method.

### A. Inverse Isoparametric Mapping Algorithm

The IIMA is a locally supported interpolation function, which uses piecewise functions to approximate each stiffener element nodal displacement using nodal displacements for one single plate element. The detailed description of the IIMA is not shown here for brevity. However, they can be found in our previous work [7,17]. For completeness, we will briefly explain this method.

Consider the mesh for a curvilinearly stiffened plate, as shown in Fig. 3a. The displacement field for each node of the stiffener beam elements can be approximated using nodal displacements for a single plate element. This is accomplished by using finite element shape functions. For isoparametric shell elements, the natural coordinates used in the finite element shape functions for the spatial approximation and displacement approximation are the same. Therefore, based on the coordinates of each stiffener beam-element node and plate-element nodes, one can find out the plate element where each stiffener beam-element node is located and then compute the corresponding natural coordinates. After that, the natural coordinates will be used to compute the finite element shape functions for each stiffener beam-element nodal displacement approximation. Repeat the process for all stiffener beam-element nodes. All nodal displacements for the stiffeners can be obtained and written in a matrix form as

$$\{\mathbf{d}_{sg}\} = [\mathbf{N}_{sp}]\{\mathbf{d}_p\} \quad (9)$$

where  $\mathbf{d}_{sg}$  and  $\mathbf{d}_p$  are vectors for the stiffener and plate-element nodal displacements described in the global coordinate system, respectively.

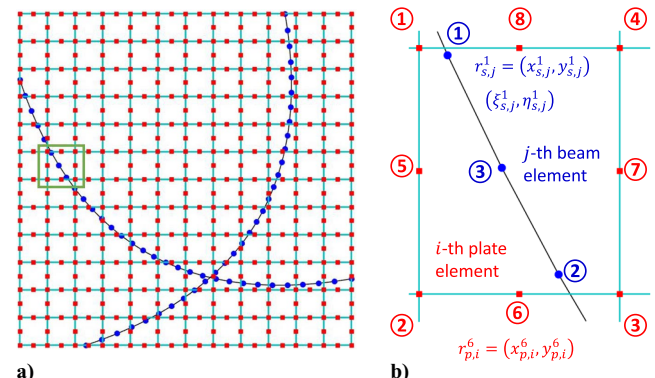


Fig. 3 Nonconformal mesh modeling of a stiffened plate.

## B. Radial Basis Function

A globally continuous and differentiable RBF is used as an interpolation function for approximating each stiffener beam-element nodal displacement using all plate-element nodal displacements, which is expressed as

$$u_{sg}(r_s) = \sum_{j=1}^n a_j \phi(\|r_s - r_{p,j}\|) + p(r_s) \quad (10)$$

where  $u_{sg}(r_s)$  is the stiffener nodal displacement described in the global coordinate system, representing the same DOF of the stiffener displacement field vector  $\mathbf{d}_{sg}$ ;  $r$  represents the coordinates for any node,  $r = (x, y, z)$ ;  $r_s$  is stiffener beam-element node coordinate;  $a_j$  is the coefficient for the  $j$ th RBF, and  $n$  is the number of the plate-element nodes;  $r_{p,j}$  are the center points for the RBFs, representing the  $j$ th node coordinate for the plate element in the present work; and  $\phi(\|r_s - r_{p,j}\|)$  is the basis function with respect to the Euclidean distance,  $\|r_s - r_{p,j}\|$ . In this study, we select two representative basis functions: 1)  $C^2$  Wendland function and 2) MQ function. When the interpolation matrix computed using the chosen basis function  $\phi$  is not positive definite, the lower-order polynomials are required [41]. The function  $p(r)$  are lower-order polynomials as compared to the basis functions that are not present in the basis functions [41,42].

The coefficients  $a_j$  and polynomial  $p(r)$  given in Eq. (10) are determined using

$$u_{sg}(r_{p,j}) = u_{p,j} \quad (11a)$$

$$\sum_{j=1}^n a_j p(r_{p,j}) = 0 \quad (11b)$$

Here, Eq. (11a) shows that the interpolated displacement obtained using the RBFs at the plate-element nodes should be the same as the plate-element node displacement,  $u_{sg}(r_{p,j}) = u_{p,j}$ . Equation (11b) represents the condition of orthogonality should be satisfied.

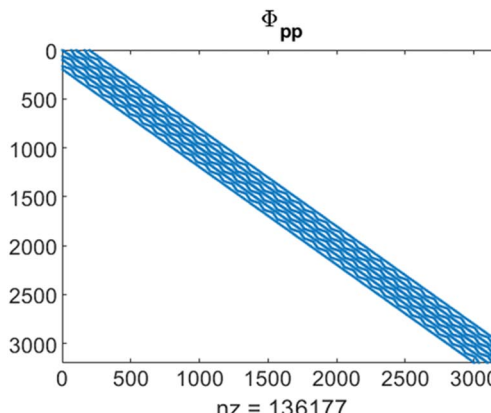
### 1. $C^2$ Wendland Function

The  $C^2$  Wendland basis function is a positive definite function [42,43]. The lower-order polynomials  $p$  given in Eq. (10) are not considered. Equation (11a) can be expressed in a matrix form to compute the coefficient vector  $\mathbf{a}$  as used in Eq. (10), which is expressed as

$$\{\mathbf{u}_p\} = [\Phi_{pp}]\{\mathbf{a}\} \quad (12)$$

where

$$\Phi_{pp} = \begin{bmatrix} \phi(\|r_{p,1} - r_{p,1}\|) & \phi(\|r_{p,1} - r_{p,2}\|) & \dots & \phi(\|r_{p,1} - r_{p,n}\|) \\ \phi(\|r_{p,2} - r_{p,1}\|) & \phi(\|r_{p,2} - r_{p,2}\|) & \dots & \phi(\|r_{p,2} - r_{p,n}\|) \\ \vdots & \vdots & \ddots & \vdots \\ \phi(\|r_{p,n} - r_{p,1}\|) & \phi(\|r_{p,n} - r_{p,2}\|) & \dots & \phi(\|r_{p,n} - r_{p,n}\|) \end{bmatrix}_{n \times n}$$



and  $n$  is the number of plate shell element nodes, and the  $C^2$  Wendland basis function  $\phi$  shown in the preceding matrix is expressed as

$$\phi(\|\mathbf{x}\|) = \begin{cases} \left(1 - \frac{\|\mathbf{x}\|}{r_{max}}\right)_+^4 \cdot \left(4 \frac{\|\mathbf{x}\|}{r_{max}} + 1\right) & \text{if } \|\mathbf{x}\| \leq r_{max} \\ 0 & \text{otherwise} \end{cases} \quad (13)$$

where the Euclidean distance is  $\|\mathbf{x}\| = \|r_{p,i} - r_{p,j}\|$ , and the support radius  $r_{max}$  is used to select the neighboring plate-element nodes to approximate the present stiffener beam-element nodal displacement.

The coefficient vector  $\mathbf{a}$  given in Eq. (12) can be obtained as

$$\{\mathbf{a}\} = [\Phi_{pp}]^{-1}\{\mathbf{u}_p\} \quad (14)$$

Substitute Eq. (14) to Eq. (10) and ignore the lower-order polynomial, the stiffener nodal displacement  $u_{sg}$  can be approximated using the plate nodal displacement  $\mathbf{u}_p$  as

$$\{u_{sg}\} = [\Phi_{sp}]\{\mathbf{a}\} = [\Phi_{sp}][\Phi_{pp}]^{-1}\{\mathbf{u}_p\} \quad (15)$$

where

$$\Phi_{sp} = \begin{bmatrix} \phi(\|r_{s,1} - r_{p,1}\|) & \phi(\|r_{s,1} - r_{p,2}\|) & \dots & \phi(\|r_{s,1} - r_{p,n}\|) \\ \phi(\|r_{s,2} - r_{p,1}\|) & \phi(\|r_{s,2} - r_{p,2}\|) & \dots & \phi(\|r_{s,2} - r_{p,n}\|) \\ \vdots & \vdots & \ddots & \vdots \\ \phi(\|r_{s,m} - r_{p,1}\|) & \phi(\|r_{s,m} - r_{p,2}\|) & \dots & \phi(\|r_{s,m} - r_{p,n}\|) \end{bmatrix}_{m \times n}$$

$m$  is the number of stiffener element nodes.

For simplicity, Eq. (15) can be written as

$$\{u_{sg}\} = [\mathbf{H}_{sp}]\{\mathbf{u}_p\} \quad (16)$$

where  $\mathbf{H}_{sp} = [\Phi_{sp}][\Phi_{pp}]^{-1}$ .

The matrices for  $C^2$  Wendland function-based RBF,  $\Phi_{sp}$  or  $\Phi_{pp}$ , remain sparse but not the interpolation matrix  $\mathbf{H}_{sp}$ . The two matrices,  $\Phi_{sp}$  or  $\Phi_{pp}$ , used in the example studied in Sec. IV are plotted in Fig. 4, where the support radius is twice the element length of the plate model. Although  $\Phi_{sp}$  or  $\Phi_{pp}$  are sparse matrices, the sparsity of the interpolation matrix  $\mathbf{H}_{sp}$  used in the structural analysis is not guaranteed, which will be investigated in Sec. IV.

Equation (16) shows the stiffener nodal displacement approximation in terms of the plate-element nodal displacement using RBFs. In this study, each node has six DOFs, the expression for  $N_{sp}$ , as given in Eqs. (2), (6), and (8), is shown as

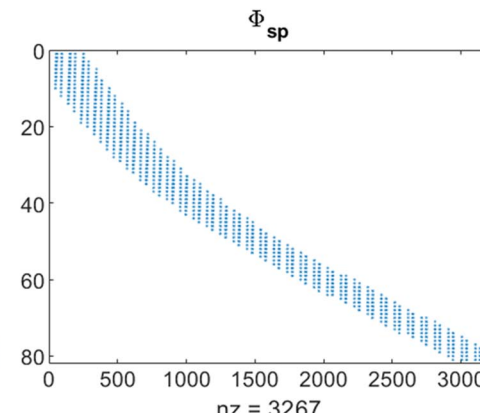


Fig. 4 Sparsity of matrices  $\Phi_{pp}$  and  $\Phi_{sp}$  using  $C^2$  Wendland function-based RBF.

$$N_{sp} = \begin{bmatrix} \mathbf{H}_{sp} & 0 & 0 & 0 & 0 & 0 \\ 0 & \mathbf{H}_{sp} & 0 & 0 & 0 & 0 \\ 0 & 0 & \mathbf{H}_{sp} & 0 & 0 & 0 \\ 0 & 0 & 0 & \mathbf{H}_{sp} & 0 & 0 \\ 0 & 0 & 0 & 0 & \mathbf{H}_{sp} & 0 \\ 0 & 0 & 0 & 0 & 0 & \mathbf{H}_{sp} \end{bmatrix} \quad (17)$$

## 2. MQ Function

Another commonly used MQ function is also considered as the basis function for the RBF due to the overall best performance [44], which is expressed as

$$\phi_i(\mathbf{r}) = \sqrt{(\mathbf{r} - \mathbf{r}_i)^2 + c_i^2} \quad (18)$$

where  $c_i$  is the free shape parameter, which is commonly assumed to be constant for all discrete points in most applications [45,46];  $\mathbf{r}$  are the nodal coordinates,  $\mathbf{r} = (x, y, z)$ . The physical foundation of MQ splines is that MQ is related to a consistent solution of the biharmonic potential problem [47]. Micchelli [48] pointed out that the MQ collocation matrices are conditional positive definiteness, therefore, lower order polynomials are considered in the interpolation functions [49] for a complete approximation function. For a 2-D structure problem, the linear polynomial is selected and expressed as  $\beta_0 + \beta_1 x + \beta_2 y$ . Based on Eq. (11), we can determine the coefficient vector  $\{\beta^T \quad \alpha^T\}^T$  from

$$\begin{bmatrix} \mathbf{0} & \mathbf{P}_p^T \\ \mathbf{P}_p & \Phi_{pp} \end{bmatrix} \begin{Bmatrix} \beta \\ \alpha \end{Bmatrix} = \begin{Bmatrix} \mathbf{0} \\ \mathbf{u}_p \end{Bmatrix} \quad (19)$$

where

$$\Phi_{pp} = \begin{bmatrix} \phi_{11} & \phi_{12} & \dots & \phi_{1n} \\ \phi_{21} & \phi_{22} & \dots & \phi_{2n} \\ \vdots & \vdots & \ddots & \vdots \\ \phi_{n1} & \phi_{n2} & \dots & \phi_{nn} \end{bmatrix}_{n \times n} \quad \mathbf{P}_p = \begin{bmatrix} 1 & x_{p,1} & y_{p,1} \\ 1 & x_{p,1} & y_{p,1} \\ \vdots & \vdots & \vdots \\ 1 & x_{p,n} & y_{p,n} \end{bmatrix}_{n \times 3}$$

where

$$\phi_{ij}(\mathbf{r}_{p,i}) = \sqrt{(\mathbf{r}_{p,i} - \mathbf{r}_{p,j})^2 + c_j^2} \quad (20)$$

Unlike the sparse basis function matrix obtained using  $C^2$  Wendland function-based RBF shown in Fig. 4, the present  $\Phi_{pp}$  is a fully populated matrix when the shape parameter  $c_j$  is not zero.

The coefficients  $\alpha$  and  $\beta$  can be solved based on Eq. (19). After that, based on Eq. (10), the displacement for each stiffener element node can be approximated using all plate-element nodal displacements:

$$\begin{aligned} \{\mathbf{u}_{sg}\} &= [\mathbf{P}_s \quad \Phi_{sp}] \begin{Bmatrix} \beta \\ \alpha \end{Bmatrix} = [\mathbf{P}_s \quad \Phi_{sp}] \begin{bmatrix} \mathbf{0} & \mathbf{P}_p^T \\ \mathbf{P}_p & \Phi_{pp} \end{bmatrix}^{-1} [\mathbf{T}_p] \{\mathbf{u}_p\} \\ &= [\mathbf{H}_{sp}] \{\mathbf{u}_p\} \end{aligned} \quad (21)$$

where

$$\Phi_{sp} = \begin{bmatrix} \phi_{11} & \phi_{12} & \dots & \phi_{1n} \\ \phi_{21} & \phi_{22} & \dots & \phi_{2n} \\ \vdots & \vdots & \ddots & \vdots \\ \phi_{m1} & \phi_{m2} & \dots & \phi_{mn} \end{bmatrix}_{m \times n} \quad \mathbf{P}_s = \begin{bmatrix} 1 & x_{s,1} & y_{s,1} \\ 1 & x_{s,1} & y_{s,1} \\ \vdots & \vdots & \vdots \\ 1 & x_{s,m} & y_{s,m} \end{bmatrix}_{m \times 3}$$

and

$$\phi_{ij}(\mathbf{r}_{s,i}) = \sqrt{(\mathbf{r}_{s,i} - \mathbf{r}_{p,j})^2 + c_j^2} \quad (22)$$

and  $\mathbf{T}_p$  is a selection matrix, which is expressed as

$$\mathbf{T}_p = \begin{bmatrix} 0 & 0 & \dots & 0 \\ 0 & 0 & \dots & 0 \\ 0 & 0 & \dots & 0 \\ 1 & 0 & \dots & 0 \\ 0 & 1 & \dots & 0 \\ \vdots & \vdots & \ddots & \vdots \\ 0 & 0 & \dots & 1 \end{bmatrix}_{(n+3) \times n}$$

The expression for  $N_{sp}$ , as given in Eqs. (2), (6), and (8), can be determined using  $\mathbf{H}_{sp}$  obtained from Eq. (21).

## C. TPS Method

The TPS method is based on the bending of a thin-plate model [50], and each nodal displacement for the stiffener beam elements is written as

$$u = \sum_{i=1}^n (\alpha_i |\mathbf{r} - \mathbf{r}_i|^2 \log |\mathbf{r} - \mathbf{r}_i|) + \beta_0 + \beta_1 x + \beta_2 y \quad (23)$$

where  $u$  is the stiffener nodal displacement;  $\mathbf{r}$  is the stiffener node coordinate;  $\mathbf{r}_i$  is the  $i$ th plate-element nodal coordinate;  $n$  is the number of total plate-element nodes; and  $(x, y)$  are the coordinates of any point within the plate, either the stiffener element nodal coordinate or the plate-element nodal coordinate.

There are  $n + 3$  unknown coefficients,  $\alpha_i$  ( $i = 1, 2, \dots, n$ ) and  $\beta_0$ ,  $\beta_1$ , and  $\beta_2$  given in Eq. (23). In addition to  $n$  equations based on Eq. (11a), there are three additional equilibrium equations (force and moment equilibrium for the present thin plate in bending motion):

$$\sum_{i=1}^n \alpha_i = \sum_{i=1}^n \alpha_i x_i = \sum_{i=1}^n \alpha_i y_i = 0 \quad (24)$$

After solving the coefficients, one can substitute them to Eq. (23) for displacement of each stiffener beam-element node. Like the methods explained in the preceding section to obtain the approximation matrix, as shown in Eq. (17), we can obtain the matrices  $\mathbf{H}_{sp}$  and  $N_{sp}$  using the TPS method. The method has been documented in detail in Ref. [50], which will not be shown here for brevity.

## IV. Buckling of Composite Plate with Tow-Fiber-Path Laminates and Curvilinear Stiffeners

The improved six-DOF finite element modeling and the four different skin–stringer connection approaches, including the IIMA, two different RBFs, and the TPS method presented in Sec. III, are first employed to conduct buckling analysis of a previously studied model. The buckling mode results and computational time are compared and discussed. Additionally, the distributions of the displacement approximation matrices computed using the four different skin–stringer connection approaches are investigated.

### A. Description of the Studied Model

A previously studied curvilinearly stiffened varying-angle tow (VAT) laminated plate with four stiffeners [39], as shown in Fig. 5a, is employed in this study. Tow-steered lamina with nonlinearly varying (NLV) fiber-path orientations is considered for each layer of the squared composite plate. The curved fiber path for the VAT laminated plate is defined by using Lagrangian polynomials, which is given in Ref. [21]. The laminate configuration for the 16-layer composite plate is denoted as  $[\pm \Theta_1, \pm \Theta_2]_{2,s}$ . The layer thickness is

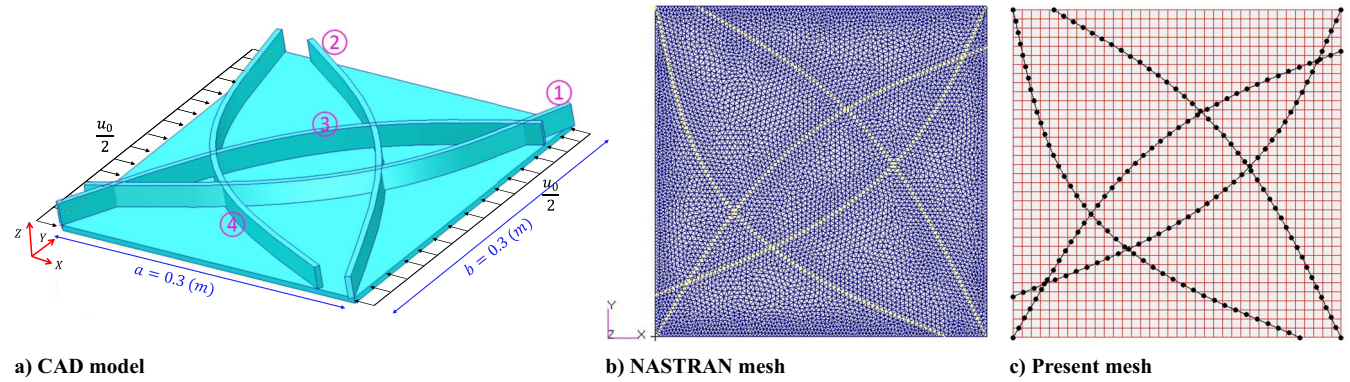


Fig. 5 Square panel with NLV fiber-path laminates and four arbitrarily shaped stiffeners [39].

Table 1 Material properties [39]

Property	Value
$E_1$	181 GPa
$E_2$	10.27 GPa
$\nu_{12}$	0.28
$G_{12}$	7.17 GPa

$1.272 \times 10^{-4}$  m. The material properties are shown in Table 1. The four stiffener curves are generated by using the Hobby spline shown in Fig. 5a. The depth ratio for the blade stiffener, defined as the ratio of the height over the width, is 5 for the studied model. The width of the cross section equals the plate total thickness. The material properties for the stiffeners are the same and are shown in Table 1. The stiffener is modeled as an orthotropic composite beam model.

A uniform axial end shortening is applied on the panel edges 1)  $X = 0, u = (\Delta u_0/2)$  and 2)  $X = a, u = -(\Delta u_0/2)$  (see Fig. 5a), where  $a$  is the panel's length along the  $X$  axis and  $\Delta u_0 = 0.02$  mm. The other boundary conditions in the pre-buckling analysis are 1)  $Y = (0, b), v_0 = 0$  and 2)  $w = 0$  for four edges. Here,  $b$  is the plate's width along the  $y$  axis. For the buckling analysis, a simply supported boundary condition is considered,  $u = v = w = 0$ , for the four panel edges. For an accurate representation of the stiffener geometry using discrete points, we used 80 beam elements for each stiffener. The plate is modeled by using  $32 \times 32$  eight-node shell elements.

### B. Discussion of Buckling Mode Results Computed Using Different Skin-Stringer Connection Approaches

Although the first buckling mode is of interest in the structural design, we compare the first four buckling mode results against previous results [39], as shown in Tables 2 and 3 for a stiffened plate with concentric and eccentric stiffeners, respectively. Eccentricity is

Table 2 Comparison of buckling eigenvalues of the curvilinearly stiffened plate with concentric stiffeners ( $e = 0$ )

Mode no.	NASTRAN [39]	IIMA	RBF $C^2$ Wendland function					RBF MQ function				TPS
			$r = 1\Delta^a$	$r = 2\Delta$	$r = 5\Delta$	$r = 10\Delta^b$	$r = 100\Delta$	$c = 0.0001^b$	$c = 0.01$	$c = 0.1$	$c = 1$	
1	7.29	7.16 (7.09) <sup>c</sup>	18.71	7.65	7.17	7.15	7.15	7.15	7.13	32.93	43.38	7.14
2	12.66	12.47 (12.39)	21.33	12.57	12.46	12.45	12.45	12.48	12.43	33.69	46.63	12.44
3	15.92	15.51 (15.31)	21.83	15.59	15.47	15.46	15.45	15.50	15.41	35.06	52.18	15.45
4	16.48	16.15 (16.00)	25.43	16.17	16.11	16.11	16.11	16.16	16.07	36.52	53.42	16.11
Total CPU time $t_c^e$	—	—	1.00	—	—	2.04	—	2.10	—	—	—	2.07
$t_c$ for $N_{sp}^c$ [see Eq. (17)]	—	—	0.50	—	—	0.06	—	0.19	—	—	—	0.09
$t_c$ for structural analysis, <sup>c,d</sup>	—	—	0.50	—	—	1.99	—	1.92	—	—	—	2.07

<sup>a</sup> $\Delta$  is the element length of the plate, rounded to  $\Delta = 0.01$  mm.

<sup>b</sup>Selected in the subsequent mode shape comparison.

<sup>c</sup>All times are normalized about the total CPU time using IIMA.

<sup>d</sup>Total CPU time, excluding the time for interpolation matrix computation.

<sup>e</sup>Values in brackets are obtained from the previous five-DOF modeling approach [39].

Table 3 Comparison of buckling eigenvalues of the curvilinearly stiffened plate with eccentric stiffeners ( $e = (1/2)(h_s + t_p)$ )

Mode no.	NASTRAN [39]	IIMA	RBF $C^2$ Wendland function					RBF MQ function				TPS
			$r = 1\Delta^a$	$r = 2\Delta$	$r = 5\Delta$	$r = 10\Delta^b$	$r = 100\Delta$	$c = 0.0001^b$	$c = 0.01$	$c = 0.1$	$c = 1$	
1	14.91	14.91 (14.70) <sup>c</sup>	18.80	14.95	14.84	14.83	14.83	14.92	14.79	38.65	60.17	14.85
2	17.85	17.85 (17.50)	22.08	17.84	17.76	17.75	17.75	17.86	17.69	40.05	61.48	17.78
3	20.80	20.84 (20.44)	22.61	20.76	20.76	20.76	20.76	20.85	20.72	41.06	62.76	20.78
4	22.89	22.69 (22.32)	27.07	22.71	22.54	22.53	22.53	22.72	22.43	42.42	64.80	22.58
Total CPU time $t_c^e$	—	—	1	—	—	2.50	—	2.68	—	—	—	2.52
$t_c$ for $N_{sp}^c$ [see Eq. (17)]	—	—	0.49	—	—	0.06	—	0.18	—	—	—	0.09
$t_c$ for structural analysis <sup>c,d</sup>	—	—	0.51	—	—	2.44	—	2.50	—	—	—	2.43

<sup>a</sup> $\Delta$  is the element length of the plate, rounded to  $\Delta = 0.01$  mm.

<sup>b</sup>Selected in the subsequent mode shape comparison.

<sup>c</sup>All times are normalized about the total CPU time using IIMA.

<sup>d</sup>Total CPU time, excluding the time for interpolation matrix computation.

<sup>e</sup>Values in brackets are obtained from the previous five-DOF modeling approach [39].

defined as the distance between the centroids of the plate and the stiffener; for the eccentric stiffener, the eccentricity distance  $e = (1/2)(t_p + h_s)$ , where  $t_p$  and  $h_s$  are the plate thickness and the stiffener cross-sectional height, respectively. For the concentric stiffener,  $e = 0$ . The buckling mode shapes for the first four modes for the stiffened plates with concentric and eccentric stiffeners are shown in Figs. 6 and 7, respectively.

The IIMA-based buckling mode results using six-DOF for each node of the stiffened plate are found to be in a better agreement with the NASTRAN results than the previous five-DOF modeling approach [39]. The buckling load factors of the curvilinearly stiffened VAT

laminated plate using the TPS function-based nonconformal mesh modeling are also close to those obtained using NASTRAN [21] and the IIMA. Conformal mesh is considered in the NASTRAN FEM, where the stiffener and the plate are modeled as beam and shell elements, respectively.

When using the  $C^2$  Wendland function as the basis function for the RBF, as suggested by Wei et al. [22], the support radius  $r_{\max}$  is 2.2 times of the element length  $\Delta$ . In this work, we are using uniform mesh for the plate; the minimal element size of the plate is chosen as  $\Delta = 0.01$  m, and the support radius is 0.022 m. We also considered different support radius values to investigate their effects on the

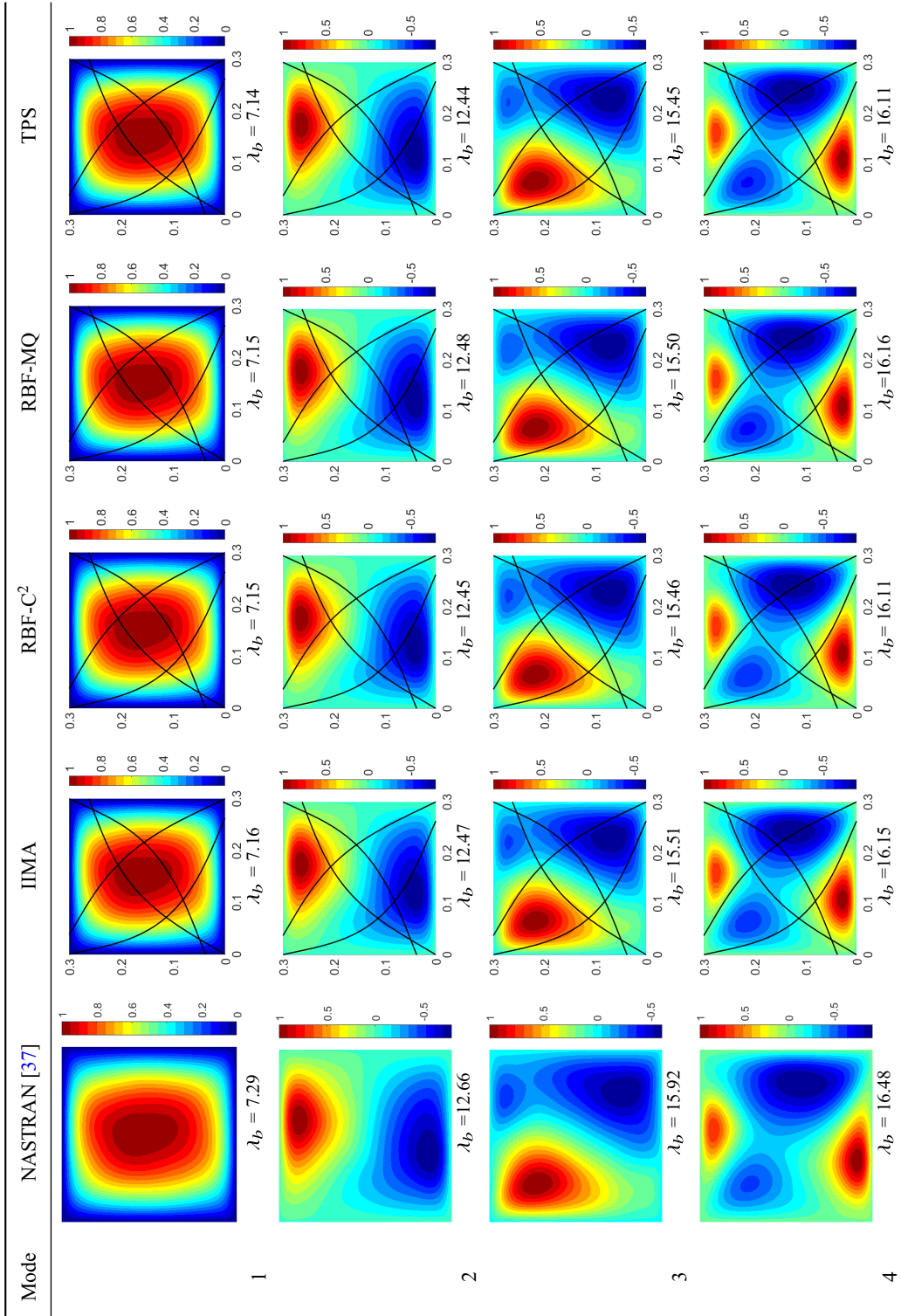


Fig. 6 Comparisons of buckling results for curvilinearly stiffened VAT laminates with concentric stiffeners.

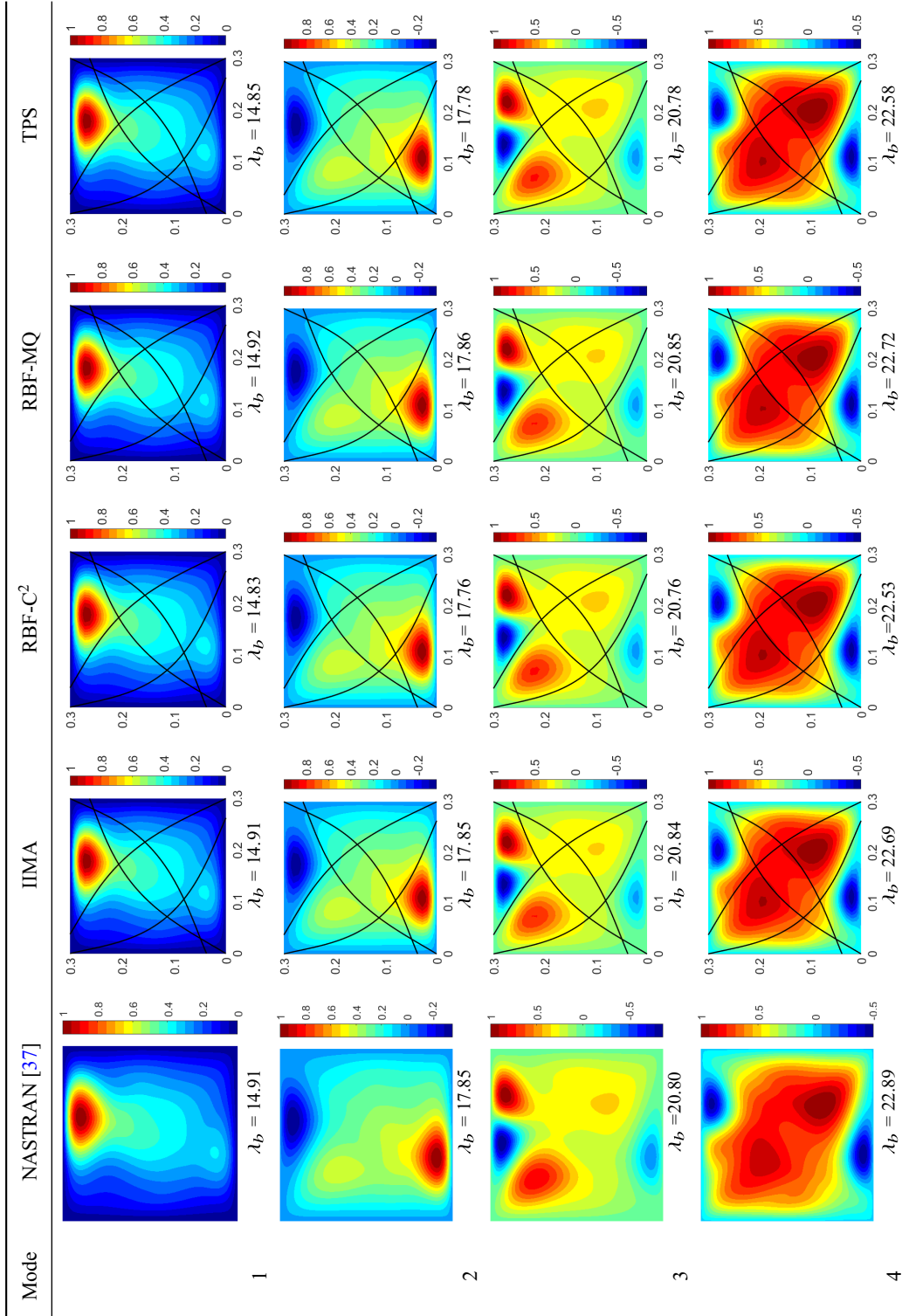


Fig. 7 Comparisons of buckling results for curvilinearly stiffened VAT laminates with eccentric stiffeners.

buckling mode results. Tables 2 and 3 show that the buckling load factors get converged with the support radius, and the converged results match well with the previous results [39]. Parametric studies show that it is better to choose a larger support radius for the  $C^2$  Wendland function when using it as the basis functions for RBF. However, a larger radius will lead the two intermediate matrices (see Fig. 4) close to fully populated.

When using the MQ function as the basis function for the RBF, one needs to choose a proper shape parameter  $c$  as used in the MQ function [see Eq. (18)]. Wang and Wang [49] used two different shape parameters (0.0001 and 1) in the topology optimization studies. In this study,

we employ four different shape parameters from 0.0001 to 1 to investigate their effect on the buckling mode results. It is found that the smaller the value of the shape parameter is, the more accurate are the buckling mode results. Note that the shape parameter used in the MQ function is not used to determine the number of neighboring plate-element nodes for the stiffener displacement approximation; it is used to change the interpolation function's shape. As pointed out by Ferreira [46], the MQ solution depends on the choice of the shape parameter, a user-defined parameter. From the present study, it is suggested to use the smallest shape parameter value for the MQ function-based RBF when using it for nonconformal mesh modeling of stiffened plates.

The first four buckling mode shapes are examined, as shown in Figs. 6 and 7. For the buckling mode shapes computed using RBF with  $C^2$  Wendland function, a support radius  $r = 10\Delta$  is employed. The shape parameter used in the RBF with the MQ function is very small,  $c = 1.00 \times 10^{-4}$ . The first four buckling mode shapes computed using different skin–stringer connection approaches are almost identical to each other, which demonstrates that for the stiffened plate models studied in this section, the present approaches can interpolate the stiffener displacement in an accurate way to satisfy the displacement compatibility at the interface between the plate and the stiffeners for the buckling analysis of a stiffened plate with dissimilar mesh at the interfaces between the stiffeners and the plate.

### C. Displacement Approximation Matrix Distribution

To understand how the skin–stringer connection affects the results, we investigate the displacement approximation matrix distribution for a single point whose displacement is approximated by using all the plate nodal displacements. Figure 8a shows a single stiffener beam-element node located on the plate, whose displacement is approximated using all the plate-element nodal displacements, such as the out-of-plane deflection, as  $d_s = H_{sp}d_p = \sum_{i=1}^n H_{sp,i}d_{p,i}$ . Figure 8 shows the distribution of  $H_{sp,i}$  computed using different skin–stringer connection approaches.

Figure 8b shows the distribution of  $H_{sp,i}$  computed using the IIMA. The coefficients are not zero for the nodal displacements of

the plate element where the stiffener beam-element node is located. For other plate-element nodes, the coefficients are zeros. Considering that among all approaches, the IIMA-based buckling mode results are the most accurate (see Tables 2 and 3), whose results are mostly close to the NASTRAN traditional finite element analysis results. Therefore, the distribution of  $H_{sp,i}$  obtained using the IIMA is considered as a benchmark.

Figure 8c shows the distribution of  $H_{sp,i}$  computed using the TPS. It is seen that the interpolation matrix shape is very close to that obtained using the IIMA (Fig. 8b). However, the magnitude is different, whose maximum value is larger than that obtained from the IIMA. The coefficients corresponding to the neighboring nodes are negative; therefore, the minimum values in the TPS-based displacement approximation coefficients are not zeros.

Figures 8d–f show the distribution of  $H_{sp,i}$  computed using the RBF  $C^2$  Wendland function under different support radius values. When using the smallest support radius, the shape of the  $H_{sp,i}$  distribution is almost identical to that obtained using the IIMA (see Fig. 8b) but not the magnitude. With the increase in the support radius, more neighboring nodes are selected in the stiffener node displacement approximation. When selecting the largest support radius, it is found that the distribution of  $H_{sp,i}$  is very similar to the one obtained using TPS (see Fig. 8c) both in shape and magnitude. It is seen that the buckling mode results computed using the RBF  $C^2$  Wendland function with support radius  $r = 100\Delta$  are very close to that obtained using TPS (see Tables 2 and 3).

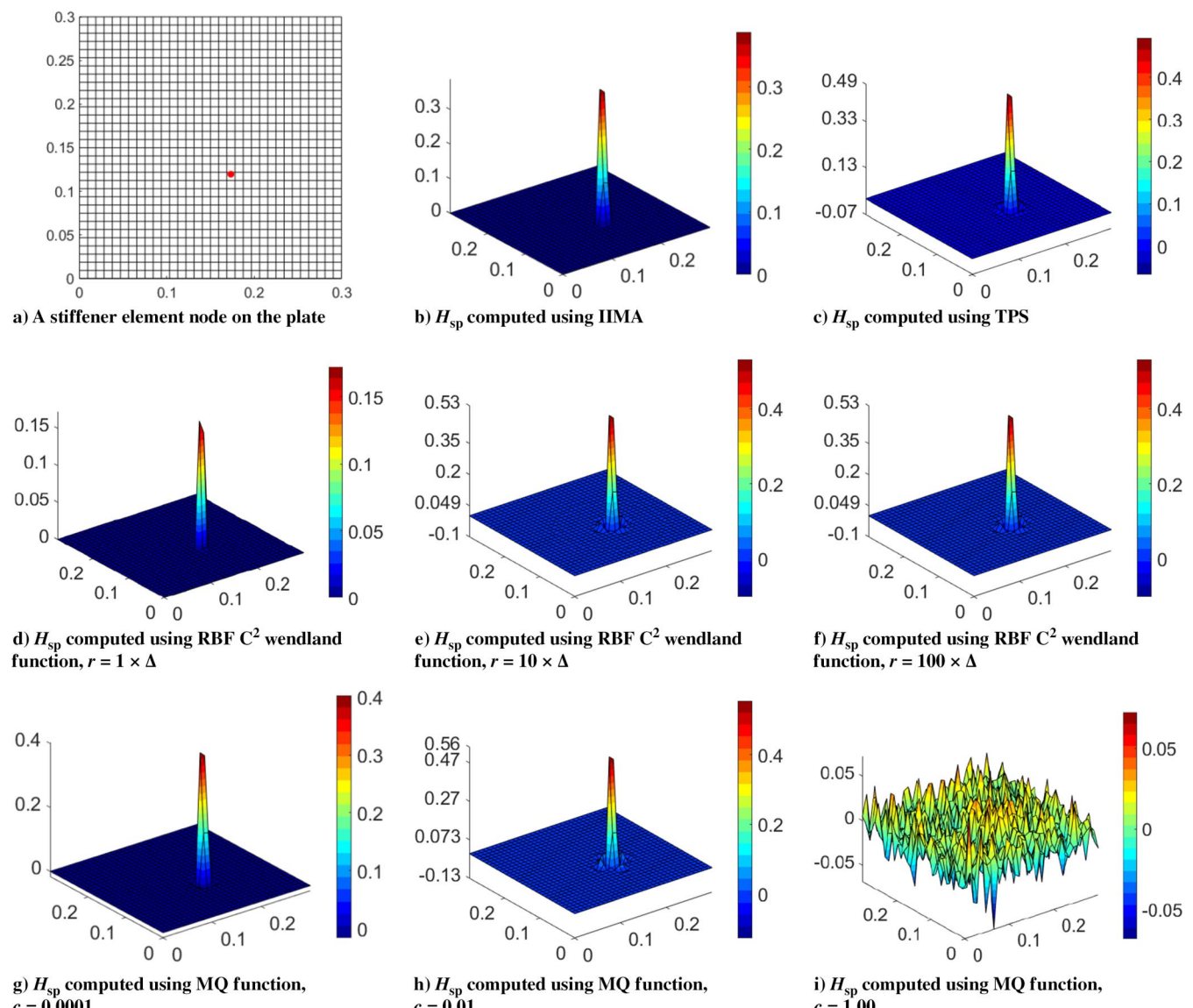


Fig. 8 Displacement approximation matrix distribution of a single point using plate's displacement field (0.173354; 0.119631).

Figures 8g–8i show the distribution of the interpolation matrix  $H_{sp}$  obtained using the RBF MQ function computed at different shape parameters. It is clearly seen that the shape parameter has a significant effect on the interpolation matrix  $H_{sp}$ . The distribution diverges as the shape parameter increases from  $1.00 \times 10^{-4}$  to 1.00. For a smaller shape parameter, the shape and magnitude of the interpolation matrix  $H_{sp}$  are very similar to that for the IIMA (see Fig. 8b). The buckling mode results computed using the RBF MQ function with a least shape parameter,  $c = 1.00 \times 10^{-4}$  and the IIMA are almost identical to each other (see Tables 2 and 3). When the shape parameter becomes larger, the shape and magnitude of the interpolation matrix become completely different. When multiplying this interpolation matrix by the stiffener stiffness matrix, the stiffener elemental stiffness will be distributed to all plate's elements rather than the one where the stiffener element is located. This will lead to an increase in all plate-element stiffness matrices. Therefore, there is an increase in the buckling load when using MQ RBF with a larger shape parameter (see Tables 2 and 3).

#### D. Comparison of Computational Time

The computational time required for computing the interpolation matrix  $N_{sp}$  [see Eq. (17)] that relates the stiffener displacement with the plate nodal displacement and the total CPU time are presented in Tables 2 and 3. The CPU time for each analysis is normalized with respect to the total CPU time for the IIMA-based analysis. The total CPU time using the RBFs and TPS approaches, which includes the computation of the interpolation matrix as well as the static and buckling analyses, is approximately twice the CPU time used by the IIMA approach.

As expected, the IIMA approach takes the most CPU time for the interpolation matrix ( $N_{sp}$ ) computation, around 50% of the total computational time, among all approaches. This is because the IIMA conducts element ID searching and root computing from high-order polynomials. The CPU time for other approaches in computing the interpolation matrices is similar, less than 10% of their respective total CPU time, which is much less than the computational time used by the IIMA approach.

The structural analysis computational time using the IIMA approach is around 50% of the total CPU time, while other approaches require

more than four times the IIMA approach computational time. This is because the interpolation matrix obtained from the IIMA still remains sparse, as seen in Fig. 9a, which results in an efficient matrix operation in the following static and buckling analyses. The interpolation matrices  $N_{sp}$  computed using the  $C^2$  Wendland function-based RBF, MQ function-based RBF, and the TPS function are not fully sparse, as seen in Figs. 9b–9d, which result in computationally expensive matrix operations during the static and buckling analyses.

## V. Buckling of a Curvilinearly Stiffened Plate with Cutouts

The stringer-skin connection approaches presented in Sec. III are all considered in this section to study the buckling mode results of curvilinearly stiffened plates with multiple cutouts [10,51,52]. This model is a representative panel of a large wing engine pylon rib, which is subjected to a combined compression-shear loading configuration that is a realistic load case. The size of the plate and the locations of the cutouts are shown in Fig. 10a. The plate and the stiffeners are all made of Al 2139-T8, whose material properties are shown in Table 4.

The stiffeners shown in Fig. 10b were obtained through design optimization by Dang et al. [10]. The stiffener shape is parameterized using three-node B-spline curves. The three control points for each B-spline curve are shown in Table 5.

The boundary conditions applied in both the static analysis and the buckling analysis are the same, which are given as 1)  $u = v = 0$  at point of  $(0, 0)$ , 2)  $u = v = 0$  at point of  $(24'', 0)$ , and 3)  $w = 0$  and in-plane drilling DOF are zeros on the four edges.

The plate thickness and stiffener sizes are shown in Table 6. All stiffeners have rectangular cross sections. The heights for all stiffener cross sections are the same, but they have different widths. Figure 11 shows the applied load condition for a compression dominant case [10] containing combined axial compression and in-plane shear loads.

The model studied in this section is also developed in Abaqus/CAE. In the Abaqus/CAE modeling, both the plate and the stiffeners are modeled as shell elements. For comparison purposes, in addition to the traditional conformal mesh-based modeling in Abaqus/CAE, we also studied two other nonconformal mesh modeling available in

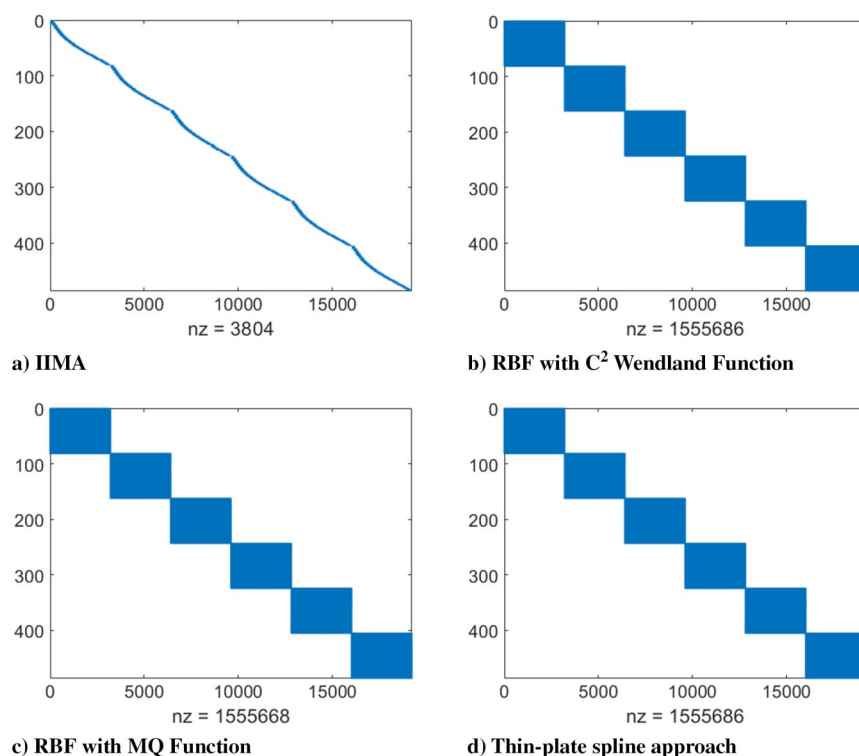


Fig. 9 Sparsity of interpolation matrix  $N_{sp}$  [see Eq. (17)], computed using different skin–stringer connection approaches.

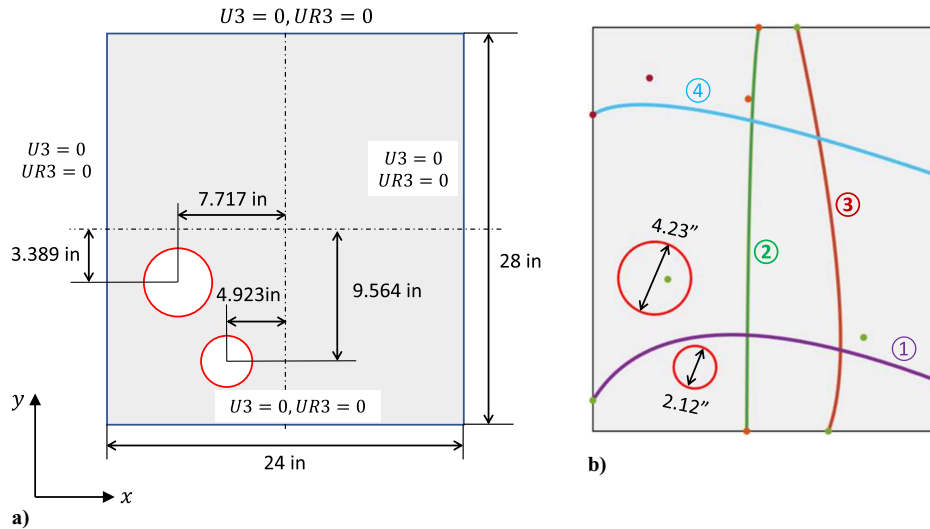


Fig. 10 Curvilinearly stiffened plate with cutouts.

**Table 4** Material properties of Al 2139-T8 [51]

Property	Value
Young's modulus $E$ , ksi	10,600
Poisson's ratio $\nu$	0.33
Yield stress, ksi	68.1

**Table 5** Three control points for each stiffener generated using B-spline curve

Stiffener No.	Control points coordinates
Stiffener 1	(0, 2.1348), (5.1949, 10.5332), (24, 3.4526)
Stiffener 2	(11.4994, 28), (10.7693, 23.0407), (10.6650, 0)
Stiffener 3	(14.1542, 28), (18.7687, 6.4965), (16.3251, 0)
Stiffener 4	(0, 21.9472), (3.9273, 24.4891), (24, 17.6943)

**Table 6** Plate thickness and stiffener size [51]

Property	Value, in.
Plate thickness	0.1160
Height for all stiffeners	0.5295
Stiffener 1 width	0.0785
Stiffener 2 width	0.2274
Stiffener 3 width	0.1839
Stiffener 4 width	0.0964

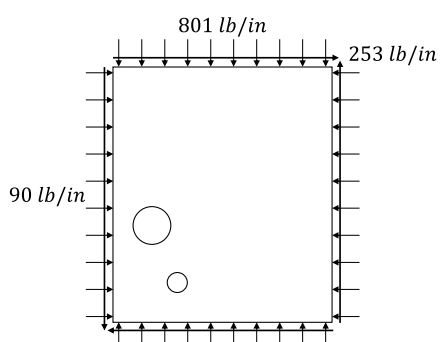


Fig. 11 Applied load boundary conditions [10], a maximum compression dominant load case.

Abaqus/CAE. A total of three different modeling approaches available in Abaqus/CAE are employed for buckling analysis of the stiffened plate with cutouts. Figure 12 shows three different modeling methods for 1) conventional (conformal mesh; Fig. 12a), 2) tie contact (nonconformal mesh; Fig. 12b), and 3) wrapping mesh approach (WMA; nonconformal mesh; Fig. 12c). All models are developed with the eight-node shell element (S8R), and the number of mesh seeds is the same for all three cases.

The first conventional approach, as seen in Fig. 12a, is a conformal mesh-based FEM. The second approach is the tie-contact method using nonconformal mesh at the stiffener/plate interface. All stiffeners are combined into a single part. The mesh configurations are separately derived for the plate and combined stiffeners. The intersection between stiffeners should be considered in the combined stiffener modeling. This means that for the combined stiffeners themselves, the conformal mesh is still considered at their interfaces. Then, we can develop the single assembly constrained with the tie contact between the primary structure, the plate, and the secondary structure, combined stiffeners, as shown in Fig. 12b. The last WMA is similar to the second one, but the stiffeners are modeled on the same plane of the plate, having the thickness as the height of the stiffener, as shown in Fig. 12c. For all stiffeners meshing in the WMA, there is no requirement to ensure a conformal mesh at the interface among all stiffeners, as opposed to the tie constraint-based nonconformal mesh approach.

Figure 13 shows the present nonconformal mesh-based FEM of a curvilinearly stiffened plate with two holes. The mesh for the plate with cutouts and all four stiffeners are generated independently. For an accurate representation of the stiffener geometry, 50 beam elements are used to model each stiffener.

Figure 14 shows the first four buckling mode results computed using Abaqus/Standard and the present method employing four different skin-stringer connection approaches. For the first two sets of Abaqus/standard results, the buckling mode results obtained using the tie-constraint mesh approach-based nonconformal mesh are very close to the conventional conformal mesh-based finite element analysis results.

The WMA-based nonconformal meshing leads to larger buckling load factors, around 4.7–7.8% difference, as compared to the results obtained using conventional shell modeling-based results. The WMA treats the stiffener height as the stiffener shell element thickness in the finite element modeling, which causes the stiffener height direction motion to be similar to a beam cross-sectional motion. As a result, this causes a larger buckling load for each mode than those obtained using other approaches. In addition, the buckling mode shape for the higher mode (mode 4) obtained using the WMA becomes slightly different from the Abaqus/Standard conventional conformal mesh-based results.

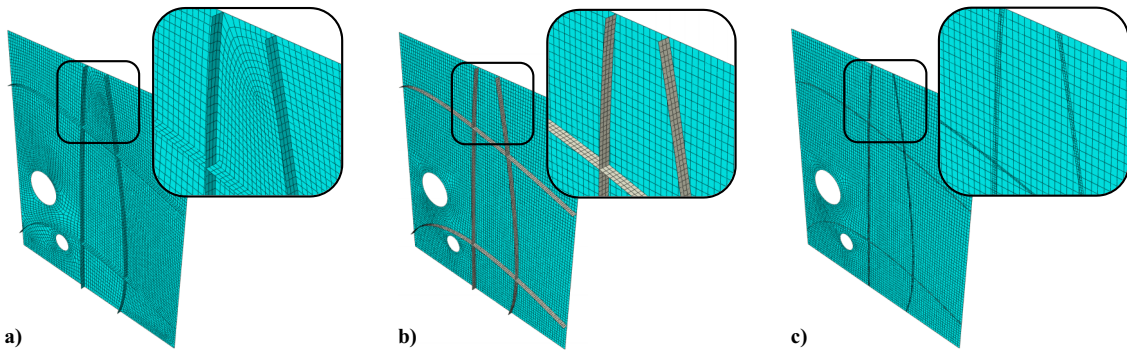


Fig. 12 Different modeling methods for stiffened plate with cutouts in Abaqus/CAE: a) conventional shell modeling, b) tie contact for intersection region, and c) WMA.

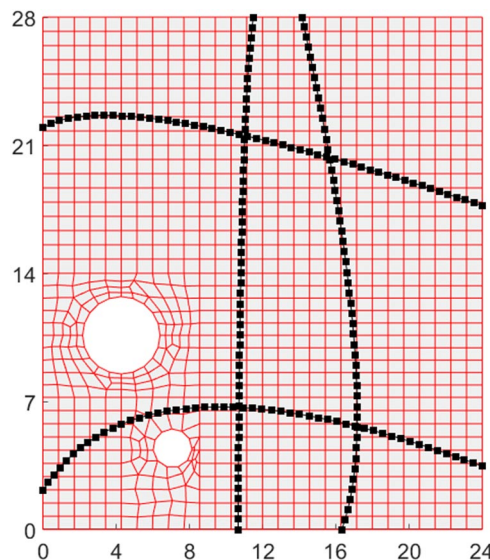


Fig. 13 Present nonconformal mesh-based FEM for curvilinearly stiffened plate with two holes.

The present buckling mode results obtained using the IIMA skin-stringer connection approach are in a good agreement with Abaqus/Standard conventional FEM-based results. When using the  $C^2$  Wendland function RBF-based skin-stringer connection approach, the support radius is considered to be  $10\Delta$ , where  $\Delta$  is the plate-element length. In the present model, we used a nonuniform mesh for the plate due to the presence of holes. Two different element sizes are studied to compute the support radius: a minimal element size length of  $\Delta_1 = 0.1427$  in. and a maximum element size length of  $\Delta_2 = 0.8578$  in. Two corresponding support radii are employed:  $r_{\max} = 10\Delta_1$  and  $r_{\max} = 10\Delta_2$ . It is clearly observed that when using a larger element length to determine the support radius  $r_{\max}$ , the buckling mode factors are close to Abaqus/standard conventional shell element-based model results in 1%. This study demonstrates that the support radius has a significant impact on the buckling mode results, which means that one needs to select a larger support radius when using the  $C^2$  Wendland function RBF-based skin-stringer connection approach.

In the case of the MQ-based RBF, the shape parameter  $c = 1.00 \times 10^{-4}$  is used. For the results presented in Fig. 14, the buckling mode shapes and buckling load factors are all close to the Abaqus/Standard results obtained using conventional shell elements for the stiffened plate with cutouts. Figure 14 also shows that the buckling mode results computed using the present method employing the TPS-based displacement approximation are close to Abaqus/Standard conventional modeling results.

Among the studied results, as shown in Fig. 14, Abaqus/CAE WMA causes a higher buckling load prediction. To investigate the further impact of the stiffener height on the buckling mode results, an additional case with deeper stiffeners for the stiffened plate is considered.

The cross-sectional height is doubled for each stiffener, as shown in Fig. 10b, resulting in a larger depth ratio, 13.5, for stiffener 1. The buckling mode results computed using different modeling approaches are shown in Fig. 14. The benchmark for comparison is provided by the buckling mode results computed using the Abaqus/CAE conventional conformal mesh-based finite element method, while the results of other approaches are compared against the benchmark.

It is clearly seen that for a stiffened plate with deeper stiffeners, a higher buckling load is obtained when using Abaqus/CAE WMA, resulting in an error of up to 11.3% for the first critical buckling load factor (mode 1). On the other hand, the present critical buckling load results obtained using different skin-stringer connection approaches are close to the benchmark results with a difference of less than 3.5%. The WMA models the stiffener as shell elements, whose thickness is the same as the stiffener height. Considering that the cross-sectional width is much less than its height, the WMA model for the stiffeners is equivalent to a beam model. However, the present approach using a beam model for the stiffener with different skin-stringer connection yields buckling mode results more closely with the benchmark result. This demonstrates that the present skin-stringer connection approaches are more accurate than those employed in the Abaqus/CAE WMA.

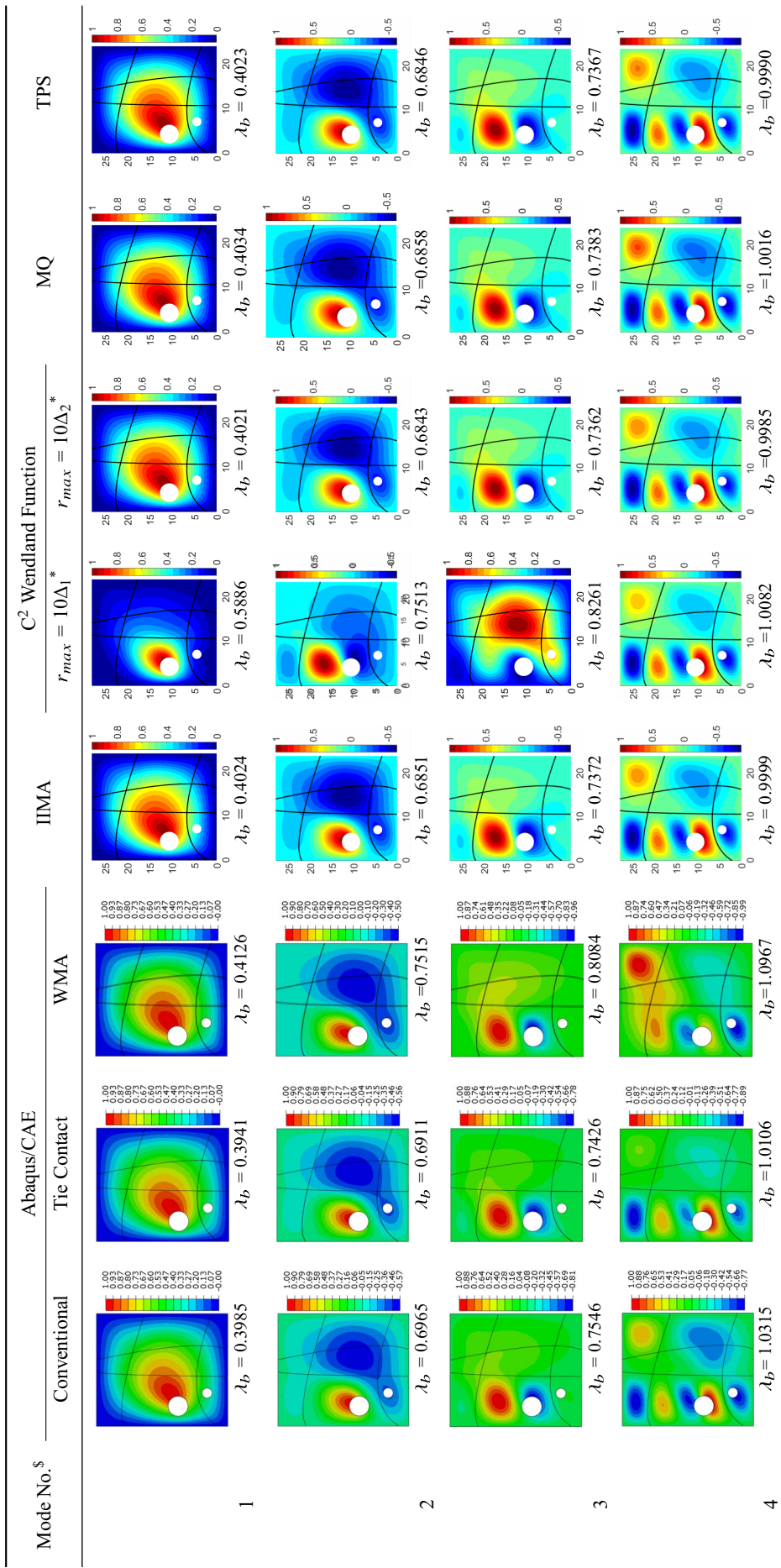
Figure 15 shows that for the present stiffened plate with deeper stiffeners, the support radius used in the  $C^2$  Wendland function RBF has a lesser impact on the buckling mode results compared to the case with lower stiffeners, as shown in Fig. 15. This further demonstrates the model dependence of the support radius when employing the  $C^2$  Wendland function RBF for the skin-stringer connection. For higher modes where local buckling mode dominates, for example, mode 4, studied in Fig. 15, the mode shapes computed using the present methods and WMA are slightly different than the modes obtained from conformal mesh-based results. This is because the present stiffener models are slightly stiffer than the stiffener shell element-based model. Nevertheless, the present buckling load factors are very close to the benchmark results within 5% for higher modes.

The present results obtained using four different skin-stringer connection approaches closely match the results obtained through Abaqus/Standard conventional and tie-contact modeling. This close correlation demonstrates the accuracy of the present nonconformal mesh-based modeling for conducting buckling analysis of curvilinearly stiffened plates with cutouts under complex load conditions. The WMA-based model leads the stiffener motion to be very similar to the present beam element-based stiffener modeling, although it uses shell elements for modeling the stiffeners. The present skin-stringer nonconformal mesh modeling and the beam element-based stiffener modeling are more accurate than the Abaqus/CAE WMA in the present study.

## VI. Curved Grid-Stiffened Variable-Angle Tow Laminated Panel

### A. Studied Model

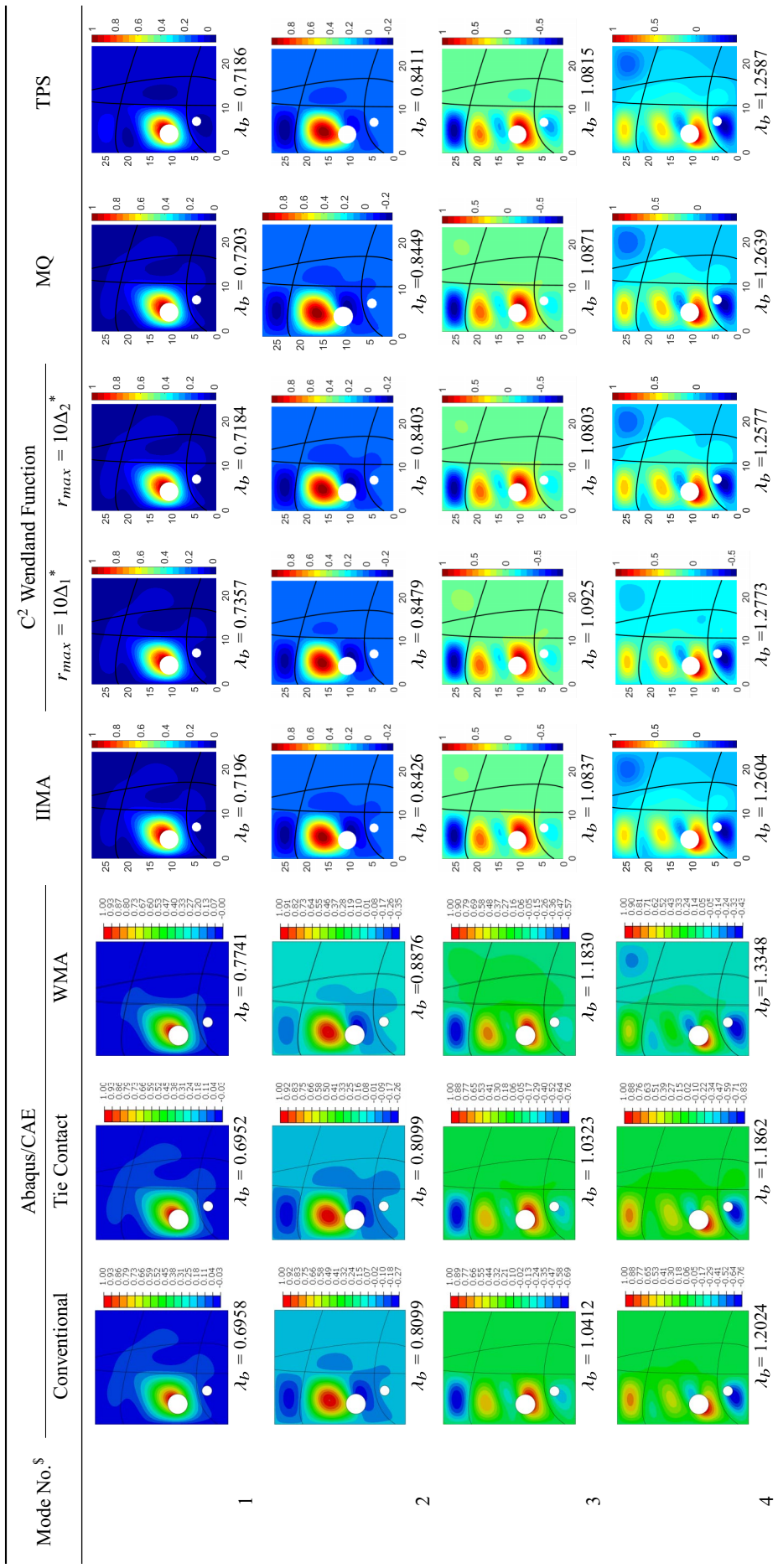
In this section, we consider applying the most efficient IIMA skin-stringer connection approach-based nonconformal mesh modeling



<sup>\$</sup>: modes for Abaqus/CAE conventional conformal-mesh based results

\* :  $\Delta_1$  and  $\Delta_2$  are, respectively, the minimum and maximum element length of the plate

Fig. 14 Comparisons of different approaches-based buckling mode results for curvilinearly stiffened plate with cutouts under compression dominant load conditions.



<sup>\$</sup>: modes for Abaqus/CAE conventional conformal-mesh based results

\*:  $\Delta_1$  and  $\Delta_2$  are, respectively, the minimum and maximum element length of the plate

Fig. 15 Buckling mode results for curvilinearly stiffened plate with cutouts with doubled stiffener height.

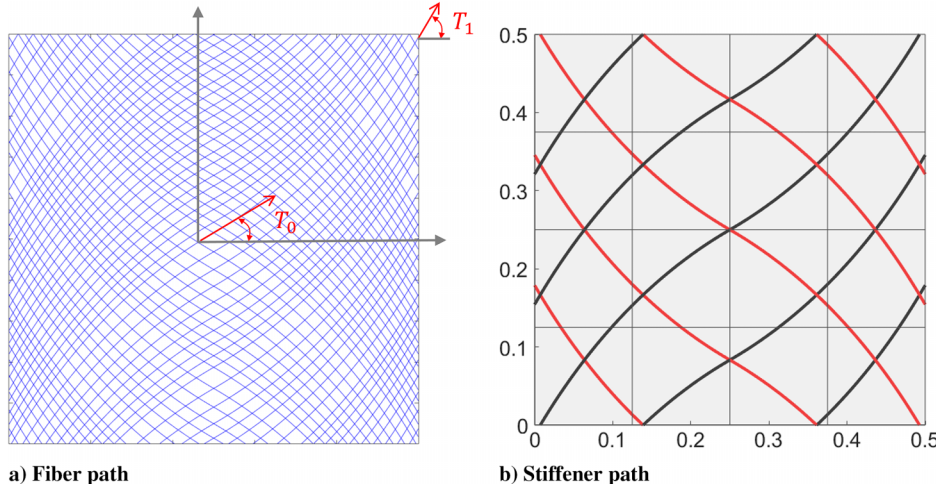


Fig. 16 Curved grid-stiffened VAT laminated panel.

for studying the buckling of a grid-stiffened plate with a spatial varying-stiffness plate model. A curvilinearly grid-stiffened VAT laminated panel [15] is considered, as shown in Fig. 16. This specific model was studied by Alhajahmad and Mittelstedt [15], where they used Abaqus/CAE WMA to study the buckling of a complex composite panel, where both spatial varying fiber path and grid stiffeners were considered. The model is therefore employed in this section for a further comparison study. The stiffener path and the fiber path are described using a function considering a linear variation of the fiber-path slope. For a linear variation of fiber-path angle along the plate length direction (i.e.,  $x$  axis), the fiber-path orientation is defined as [53]

$$\theta(x) = 2(T_1 - T_0) \left| \frac{x}{a} \right| + T_0 \quad (25)$$

where  $a$  is the length of the plate. In the center of the plate,  $x = 0$ ,  $\theta = T_0$ , and on the two edges,  $|2x/a| = 1$ ,  $\theta = T_1$ . For each layer, the fiber-path angle is denoted as  $\langle T_0 | T_1 \rangle$ . The corresponding fiber-path (curve) function is

$$y = \begin{cases} \frac{a}{2(T_1 - T_0)} \left\{ \log[\cos(T_0)] - \log \left[ \cos \left( T_0 + \frac{2}{a}(T_0 - T_1)x \right) \right] \right\}, & x \geq 0 \\ \frac{a}{2(T_1 - T_0)} \left\{ -\log[\cos(T_0)] + \log \left[ \cos \left( T_0 + \frac{2}{a}(T_0 - T_1)x \right) \right] \right\}, & x \leq 0 \end{cases} \quad (26)$$

The square VAT plate for the studied model has a side length of 500 mm. The VAT laminate configuration for the plate is given as  $[(\pm 0 \text{ deg}|75 \text{ deg})_4]_s$ . The stiffeners follow the fiber trajectories with orientations  $\pm(30 \text{ deg}|60 \text{ deg})$ . To form the grid stiffeners, the stiffener passing through the center of the plate is shifted by  $\pm L/3$  to form its adjacent stiffeners, where  $L$  is the square plate's side length. All stiffeners are projected to the plate, as shown in Fig. 16b. Both the plate and the stiffeners are made of the same materials, whose material properties are shown in Table 7.

### B. Buckling Mode Results

The present model for the grid-stiffened VAT laminated panel is shown in Fig. 17a, where the stiffeners and the plate are meshed independently. The boundary conditions and applied load are shown in Fig. 17b. All edges of the plate are required to remain straight under applied loads. This means 1) for the nodes at the edge of  $x = 0$ , all in-plane displacements along the  $x$  axis are same; 2) for the edge at  $x = L$ , all nodes have the same in-plane displacements along the  $x$  axis; 3) for the edge of  $y = L$ , all nodes have the same in-plane displacement along the  $y$  axis; 4) for nodes at  $y = 0$ , the in-plane

Table 7 Material properties of graphite-epoxy laminate [54]

Property	Value
$E_1$	155 GPa
$E_2$	12.1 GPa
$\nu_{12}$	0.248
$\nu_{13}$	0.248
$\nu_{23}$	0.458
$G_{12}$	4.4 GPa
$G_{13}$	4.0 GPa
$G_{23}$	3.2 GPa

displacement along the  $y$  axis,  $v = 0$ ; and 5) no out-of-plane displacement and no drilling rotation for the nodes on the four edges,  $w = 0$  and  $\theta_z = 0$ . The boundary conditions are the same in the static and buckling analyses.

In the study conducted by Alhajahmad and Mittelstedt [15], three different dimensions for rectangular stiffener cross sections were considered. The width  $w$  and height  $h$  of the stiffeners for each case are presented in Table 8. Concentric stiffeners were considered for the stiffened plate, meaning that the median plane of the stiffeners coincided with the median plane of the plate. The results obtained from various approaches are presented in Table 8. For the stiffened plate model, Alhajahmad and Mittelstedt [15] employed four-node shell elements (S4R) to model the skin and beam elements (B31) to represent the linearly varying grid stiffeners [54]. The Abaqus/Standard beam stiffener model uses conformal mesh for the grid-stiffened plate. In the Abaqus/CAE WMA model, the planar mesh developed at the stiffener width plane is used to build shell elements for the stiffeners. The skin was also modeled using shell elements.

The obtained results demonstrate an excellent agreement between the buckling loads computed using the present method and those obtained using the Abaqus/Standard conformal mesh-based models, where stiffeners were modeled as beams. The present results and the Abaqus/standard conformal mesh-based beam stiffener modeling results are slightly lower compared to those obtained using the Abaqus/CAE WMA. As explained by Alhajahmad and Mittelstedt [15], the slightly higher buckling load obtained from the WMA approach is due to the trimming of the stiffener planar mesh near the plate's edges. This trimming introduces slight changes in the stiffener geometry, slightly higher buckling loads are observed. The Abaqus/CAE WMA-based results for the present studied models are still very close to the conventional conformal mesh-based results. This is because the three stiffener depth ratios,  $h/w$ , are much lower than those for the stiffeners studied in Sec. V. The buckling loads computed from the present model for different grid-stiffened VAT

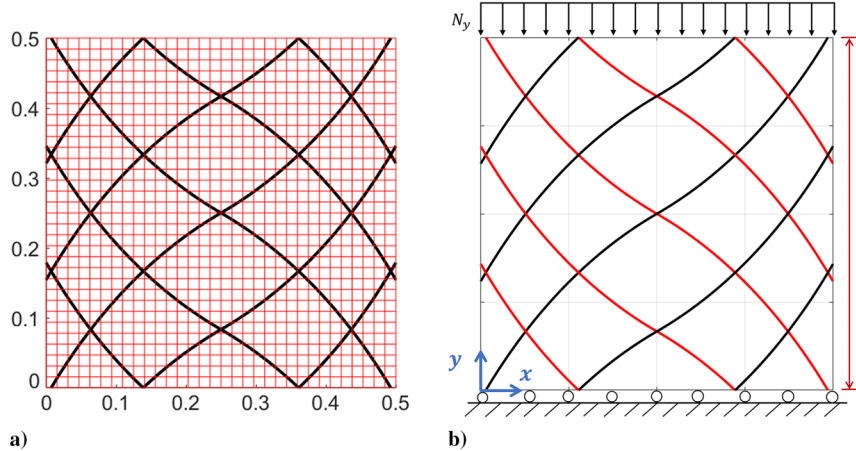


Fig. 17 Nonconformal mesh modeling of curved grid-stiffened VAT laminated panel.

**Table 8 Comparison of buckling load (N/mm) for grid-stiffened VAT laminated plates**

Source	Cross-sectional dimensions, mm		
	$h = 8; w = 2$	$h = 8; w = 8$	$h = 12; w = 6$
Present (IIMA)	155.0	240.1	401.5
Abaqus/standard beam stiffener [15]	155.4	238.2	396.5
Abaqus/CAE WMA [15]	156.7	246.6	418.9

laminated plates match well with the other two sets of results, which demonstrates the accuracy of the present method for studying the buckling of complex stiffened plate with arbitrary shape and any number of stiffeners.

## VII. Conclusions

This paper compared different skin–stringer connection approaches for studying the buckling responses of a stiffened plate with complex shape stiffeners using a nonconformal mesh-based FEM. To enforce the displacement compatibility condition at the interface between the stiffeners and the plate, the stiffener displacements are interpolated using the plate-element nodal displacements. Different interpolation functions are used, including IIMA, RBF with different basis functions, and TPS functions. Their performance in terms of buckling mode results and CPU time are compared. The present study shows that the improved six-DOF nonconformal mesh-based FEM for the stiffened plate with spatially varying-stiffness plate and arbitrarily shaped stiffeners enables an accurate buckling analysis. For the nonconformal mesh-based modeling using the RBFs for the skin–stringer connection, the buckling mode results are found to converge with the increase in the support radius as used in the  $C^2$  Wendland function. The shape parameter used in MQ function-based RBF is found to influence the buckling mode results significantly. The interpolation matrix distribution gets dispersed with an increase in the shape parameter. This aspect of the study shows that one needs to select proper parameters to be used in the basis functions when using the RBFs for the skin–stringer connection in the nonconformal mesh modeling of stiffened plates.

The nonconformal mesh modeling with different skin–stringer connection approaches shows that the IIMA takes almost 50% of its total CPU time in computing the interpolation matrix for approximating the stiffener displacements, while other methods only take less than 10% of their respective total CPU time. Nevertheless, only the interpolation matrix obtained using the IIMA remains fully sparse, resulting in the subsequent static and buckling analyses being much more efficient than the structural analysis employing the other studied skin–stringer connection approaches. In the end, the total CPU time used in structural analysis using the IIMA is around 20–25% of that obtained using the RBFs and TPS function-based skin–stringer

connection approaches, and the critical buckling loads computed using the IIMA-based nonconformal mesh modeling are close to the Abaqus/CAE conventional conformal mesh-based results less than 3.5% for all cases studied in this work.

The buckling analysis of a curvilinearly stiffened plate with four stiffeners and two holes under a very complex loading condition is studied using the present nonconformal meshing modeling and various conformal and nonconformal meshing techniques available in Abaqus/CAE. It is found that the WMA-based nonconformal meshing in Abaqus/CAE will not be accurate for stiffeners with larger heights. The present results obtained using nonconformal meshing based on four different skin–stiffener connection approaches are very close to the Abaqus/Standard conventional conformal mesh-based finite element analysis results. The present nonconformal mesh modeling with the most efficient IIMA-based skin–stringer connection method is also employed for studying the buckling of a very complex curved grid-stiffened VAT laminated plate. The present buckling mode results for the studied grid-stiffened VAT laminates with lower stiffener depth ratios are found in an excellent agreement with the Abaqus/Standard conformal mesh shell elements and the Abaqus/CAE WMA-based buckling analysis results.

The studies on the nonconformal mesh modeling using different skin–stringer connection approaches presented in this paper show that one needs to select proper values for the support radius and the shape parameter when using an RBF-based approach to approximate the stiffener nodal displacements. The TPS function is able to interpolate the stiffener nodal displacement in an accurate way but at the price of fully populated elastic and geometric stiffness matrices, resulting in an expensive structural analysis. The IIMA is the most efficient approach for the skin–stringer connection, as used in the nonconformal mesh-based modeling for the present work in terms of the accurate buckling mode results and the least CPU time.

## Appendix A: Stress–Strain Constitutive Matrix for Plate

The generalized stress resultant–strain relation for the plate can be expressed in a matrix format as

$$\begin{Bmatrix} N_x \\ N_y \\ N_{xy} \\ M_x \\ M_y \\ M_{xy} \\ Q_{xz} \\ Q_{yz} \\ M_{xz} \\ M_{yz} \end{Bmatrix} = \begin{bmatrix} [A] & [0] & [0] & [0] \\ [0] & [D] & [0] & [0] \\ [0] & [0] & [A_s] & [0] \\ [0] & [0] & [0] & [K_z] \end{bmatrix} \begin{Bmatrix} \boldsymbol{\epsilon}_{xx}^0 \\ \boldsymbol{\epsilon}_{yy}^0 \\ \boldsymbol{\gamma}_{xy}^0 \\ \boldsymbol{\kappa}_{xx}^0 \\ \boldsymbol{\kappa}_{yy}^0 \\ \boldsymbol{\kappa}_{xy}^0 \\ \boldsymbol{\gamma}_{xz}^0 \\ \boldsymbol{\gamma}_{yz}^0 \\ \boldsymbol{\kappa}_{xz} \\ \boldsymbol{\kappa}_{yz} \end{Bmatrix} \quad (A1)$$

Considering the median plane of the plate as the reference plane, that is, the centroid of the plate is located as the median plane, we can obtain the stiffness matrices as follows:

$$\mathbf{A} = t_p \frac{E}{1-\nu^2} \begin{bmatrix} 1 & \nu & 0 \\ \nu & 1 & 0 \\ 0 & 0 & \frac{1-\nu}{2} \end{bmatrix} \quad (\text{A2})$$

$$\mathbf{D} = \frac{t_p^3}{12(1-\nu^2)} \frac{E}{1-\nu^2} \begin{bmatrix} 1 & \nu & 0 \\ \nu & 1 & 0 \\ 0 & 0 & \frac{1-\nu}{2} \end{bmatrix} \quad (\text{A3})$$

where  $t_p$ ,  $E$ , and  $\nu$  are the plate thickness, material Young's modulus, and Poisson's ratio, respectively.

The out-of-plane shear constitutive relation is

$$\begin{Bmatrix} Q_{xz} \\ Q_{yz} \end{Bmatrix} = [\mathbf{A}_s] \begin{Bmatrix} \gamma_{xz}^0 \\ \gamma_{yz}^0 \end{Bmatrix} \quad (\text{A4})$$

$$\mathbf{A}_s = t_p \begin{bmatrix} G & 0 \\ 0 & G \end{bmatrix} * \mathbf{K} \quad (\text{A5})$$

where  $K$  is the shear correction factor 5/6 is used. For composite structure, the plate stiffness rigidity matrices presented in Eq. (A1) can be found in Ref. [7].

The in-plane drilling stiffness  $[\mathbf{K}_z]$  presented in Eq. (A1) is assumed to be very small but not zero to avoid a matrix singular during static and buckling analyses:

$$\mathbf{K}_z = \begin{bmatrix} 1 \times 10^{-10} & 0 \\ 0 & 1 \times 10^{-10} \end{bmatrix} E \quad (\text{A6})$$

where  $E$  is the material Young's modulus.

## Appendix B: Stress–Strain Constitutive Matrix for Stiffeners

The generalized strain field for the stiffener beam model is

$$\begin{Bmatrix} \epsilon_t^0 \\ \gamma_n^0 \\ \gamma_b^0 \\ \kappa_t^0 \\ \kappa_n^0 \\ \kappa_b^0 \end{Bmatrix} = \begin{bmatrix} \frac{d}{dx} & 0 & 0 & 0 & 0 & 0 \\ 0 & \frac{d}{dx} & 0 & 0 & 0 & -1 \\ 0 & 0 & \frac{d}{dx} & 1 & 0 & 0 \\ 0 & 0 & 0 & \frac{d}{dx} & 0 & 0 \\ 0 & 0 & 0 & 0 & \frac{d}{dx} & 0 \\ 0 & 0 & 0 & 0 & 0 & \frac{d}{dx} \end{bmatrix} \begin{Bmatrix} u_t^0 \\ v_n^0 \\ w_b^0 \\ \beta_t^0 \\ \beta_n^0 \\ \beta_b^0 \end{Bmatrix} = [\mathbf{B}_s] \{\mathbf{d}_s\} \quad (\text{B1})$$

The generalized stress resultant–strain relation for the stiffener is

$$\begin{Bmatrix} F_t \\ Q_n \\ Q_b \\ M_t \\ T_n \\ M_b \end{Bmatrix} = [\mathbf{D}_s] \begin{Bmatrix} \epsilon_t^0 \\ \gamma_n^0 \\ \gamma_b^0 \\ \kappa_t^0 \\ \kappa_n^0 \\ \kappa_b^0 \end{Bmatrix} \quad (\text{B2})$$

where

$$\mathbf{D}_s = \begin{bmatrix} EA & 0 & 0 & eEA & 0 & 0 \\ 0 & \gamma GA & 0 & 0 & eGA & 0 \\ 0 & 0 & \gamma GA & 0 & 0 & 0 \\ eEA & 0 & 0 & EI_n & 0 & 0 \\ 0 & eGA & 0 & 0 & GJ & 0 \\ 0 & 0 & 0 & 0 & 0 & EI_t \end{bmatrix} \quad (\text{B3})$$

where the bending stiffness about  $n$  axis,  $EI_n = E((1/12)b_s h_s^3 + e^2 A)$ , and  $GJ$  is the torsional rigidity. For low stiffener depth ratio,  $h_s/b_s \leq 10$ ,  $GJ = (1/3)Gh_s b_s^3 + e^2 GA$ , where  $e$  is the eccentricity, offset between the plate's median plane and the stiffener median plane,  $e = 0.5(t_p + h_s)$ . For the composite beam-based stiffeners, the cross-sectional stiffness rigidity matrix can be found in Ref. [21].

## Appendix C: Verification Studies of Modeling Stiffeners as Beams

A model studied by Stanford et al. and Townsend and Kim [37,38] is employed here to verify the accuracy of beam models for the stiffeners as used in the stiffened plate, which is shown in Fig. C1. A square thin plate has a dimension size of  $0.3 \times 0.3$  m. Three stiffeners are evenly distributed on the plate at  $y = b/4$ ,  $y = b/2$ , and  $y = 3b/4$  along the loading direction (i.e.,  $x$  axis), as seen in Fig. C1. The stiffener width  $b_s$  and the plate thickness  $t_p$  are the same; both are 1.27 mm.

For the lightweight stiffened plate as used in the wing skin structure design, the longitudinal stiffeners placed along the  $x$  axis are of interest. This is because the dominant load is the spanwise normal stress, which follows the wing's spanwise direction. To improve the buckling, the stiffeners are placed along the dominant loading direction. The boundary conditions in the verification studies are 1)  $u = v = 0$  at the edge of  $x = 0$ ; 2)  $v = 0$  at the edge of  $x = a$ ; 3)  $v = 0$  at the edges of  $y = 0, b$ ; and 4)  $w = 0$  for all four edges. Uniform distributed axial load is applied in the edge  $x = a$ ,  $N_{xx} = -1000$  N/m. The buckling load computation using the present method are compared against the commercialized finite element analysis results (i.e., NASTRAN results presented in this work). Note that when using shell elements to model the stiffeners, complex stiffener buckling mode will be occurred because the stiffener becomes very flexible in its lateral direction when the stiffener height becomes very large.

The stiffener depth ratio, defined as the ratio between the stiffener height and the stiffener width,  $\gamma = (h_s/b_s)$ , where  $h_s$  is the stiffener height, has a significant effect on the stiffened plate's buckling response. Figure C2 shows the first critical buckling load and the buckling load efficiency with the stiffener depth ratio. The buckling load efficiency refers to the ratio of the buckling load over the total structural weight. With an increase in the stiffener depth ratio, there is an increase in the buckling load and the buckling load efficiency. However, after a threshold value of the stiffener depth ratio, a further increase in the stiffener depth ratio only causes a very slight increase in the buckling load. The buckling load efficiency starts to decrease because of a larger increase in the weight with the stiffener depth

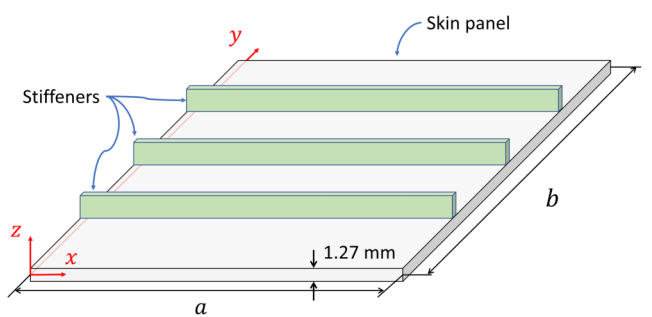


Fig. C1 Stiffened square plate with three straight stiffeners.

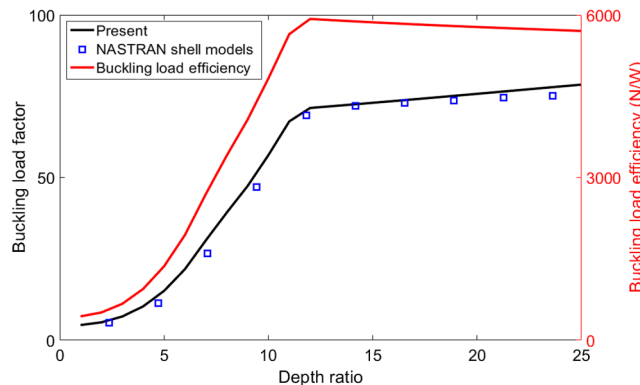


Fig. C2 Buckling load and buckling load efficiency with the stiffener depth ratio.

ratio. The buckling loads computed between the present method and the NASTRAN shell model-based results are close to each other, which demonstrates the accuracy of the present method in computing the buckling load of a stiffened plate with deep stiffeners.

### Acknowledgments

Wei Zhao would like to thank the Oklahoma State University New Faculty Startup Funding for their support. The authors also thank Ahmad Alhajahmad at Darmstadt University of Technology, Darmstadt, Germany, for helping understand the boundary conditions, as used in the model presented in Sec. VI.

### References

- [1] Havens, D., Shiyekar, S., Norris, A., Bird, R. K., Kapania, R. K., and Olliffe, R., "Design, Optimization, and Evaluation of Integrally-Stiffened Al-2139 Panel with Curved Stiffeners," NASA TM-2011-217308, 2011, <https://ntrs.nasa.gov/citations/20110023249> [retrieved 6 Nov. 2022].
- [2] Zelinski, P., "How a Solid-State Process Stood Firm Until Additive's Moment, [Online Database]," 2019, <https://www.additivemanufacturing.media/articles/how-a-solid-state-process-stood-firm-until-additives-moment> [retrieved 20 Nov. 2022].
- [3] Bedair, O., "Analysis and Limit State Design of Stiffened Plates and Shells: A World View," *Applied Mechanics Reviews*, Vol. 62, No. 2, 2009, Paper 020801. <https://doi.org/10.1115/1.3077137>
- [4] Kapania, R. K., Li, J., and Kapoor, H., "Optimal Design of Unitized Panels with Curvilinear Stiffeners," *AIAA 5th ATIO and the AIAA 16th Lighter-than-Air Systems Technology Conference and Balloon Systems Conference*, AIAA Paper 2005-7482, Sept. 2005. <https://doi.org/10.2514/6.2005-7482>
- [5] Joshi, P., Mulani, S. B., Slemp, W. C., and Kapania, R. K., "Vibro-Acoustic Optimization of Turbulent Boundary Layer Excited Panel with Curvilinear Stiffeners," *Journal of Aircraft*, Vol. 49, No. 1, 2012, pp. 52–65. <https://doi.org/10.2514/1.C031105>
- [6] Mulani, S. B., Slemp, W. C., and Kapania, R. K., "EBF3PanelOpt: An Optimization Framework for Curvilinear Blade-Stiffened Panels," *Thin-Walled Structures*, Vol. 63, Feb. 2013, pp. 13–26. <https://doi.org/10.1016/j.tws.2012.09.008>
- [7] Zhao, W., and Kapania, R. K., "Buckling Analysis of Unitized Curvilinearly Stiffened Composite Panels," *Composite Structures*, Vol. 135, Jan. 2016, pp. 365–382. <https://doi.org/10.1016/j.compstruct.2015.09.041>
- [8] Zhao, W., and Kapania, R. K., "Vibration Analysis of Curvilinearly Stiffened Composite Panels Subjected to In-Plane Loads," *AIAA Journal*, Vol. 55, No. 3, 2017, pp. 981–997. <https://doi.org/10.2514/1.J055047>
- [9] Singh, K., Zhao, W., Jrad, M., and Kapania, R. K., "Hybrid Optimization of Curvilinearly Stiffened Shells Using Parallel Processing," *Journal of Aircraft*, Vol. 56, No. 3, 2019, pp. 1068–1079. <https://doi.org/10.2514/1.C035069>
- [10] Dang, T. D., Kapania, R. K., Slemp, W. C., Bhatia, M., and Gurav, S. P., "Optimization and Postbuckling Analysis of Curvilinear-Stiffened Panels Under Multiple-Load Cases," *Journal of Aircraft*, Vol. 47, No. 5, 2010, pp. 1656–1671. <https://doi.org/10.2514/1.C000249>
- [11] Caffrey, J., and Lee, J. M., *MSC/NASTRAN 2014 Linear Static Analysis: User's Guide*, MacNeal-Schwendler, Newport Beach, CA, 2014, pp. 640–658, <https://simcompanion.hexagon.com/customers/s/article/msc-nastran-2014-linear-static-analysis-user-s-guide-doc10656> [retrieved 26 Nov. 2022].
- [12] Anon., "Mesh Tie Constraints, [Online Database]," 2016, <https://abaqus-docs.mit.edu/2017/English/SIMACAECTSTRRefMap/simacst-tiedconstraint.htm> [retrieved May 2022].
- [13] Felippa, C. A., *Introduction to Finite Element Methods*, Vol. 885, Univ. of Colorado, Boulder, CO, 2004, Chaps. 8 and 9.
- [14] Anon., "wrapMesh, [Online Database]," 2016, <http://130.149.89.49:2080/v6.14/books/ker/default.htm?startat=pt01ch18pyo02.html> [retrieved Jan. 2023].
- [15] Alhajahmad, A., and Mittelstedt, C., "Design Tailoring of Curvilinearly Grid-Stiffened Variable-Stiffness Composite Cylindrically Curved Panels for Maximum Buckling Capacity," *Thin-Walled Structures*, Vol. 157, Dec. 2020, Paper 107132. <https://doi.org/10.1016/j.tws.2020.107132>
- [16] Pidaparti, R., "Structural and Aerodynamic Data Transformation Using Inverse Isoparametric Mapping," *Journal of Aircraft*, Vol. 29, No. 3, 1992, pp. 507–509. <https://doi.org/10.2514/3.4619>
- [17] Shi, P., Kapania, R. K., and Dong, C., "Vibration and Buckling Analysis of Curvilinearly Stiffened Plates Using Finite Element Method," *AIAA Journal*, Vol. 53, No. 5, 2015, pp. 1319–1335. <https://doi.org/10.2514/1.J053358>
- [18] Shi, P., Kapania, R. K., and Dong, C., "Free Vibration of Curvilinearly Stiffened Shallow Shells," *Journal of Vibration and Acoustics*, Vol. 137, No. 3, 2015, Paper 031006. <https://doi.org/10.1115/1.4029360>
- [19] Zhao, W., Singh, K., and Kapania, R. K., "Thermal Buckling Analysis and Optimization of Curvilinearly Stiffened Plates with Variable Angle Tow Laminates," *Journal of Spacecraft and Rockets*, Vol. 54, No. 4, 2019, pp. 1–16. <https://doi.org/10.2514/1.A34378>
- [20] Liu, D., Wang, Y., Su, Z., Hao, P., Liu, X., Wang, B., and Li, G., "A New Layout Optimization Method for Stiffened Panels Based on Ground Stiffener Structure (GSS) and Thickness Penalty," *Thin-Walled Structures*, Vol. 176, July 2022, Paper 109309. <https://doi.org/10.1016/j.tws.2022.109309>
- [21] Zhao, W., and Kapania, R. K., "Skin-Stringer Assembly Using Radial Basis Functions for Curvilinearly Stiffened Panels," *AIAA Journal*, Vol. 59, No. 3, 2021, pp. 1125–1133. <https://doi.org/10.2514/1.J059364>
- [22] Wei, P., Ma, H., and Wang, M. Y., "The Stiffness Spreading Method for Layout Optimization of Truss Structures," *Structural and Multidisciplinary Optimization*, Vol. 49, No. 4, 2014, pp. 667–682. <https://doi.org/10.1007/s00158-013-1005-7>
- [23] Tamjani, A. Y., and Kapania, R. K., "Buckling and Static Analysis of Curvilinearly Stiffened Plates Using Mesh-Free Method," *AIAA Journal*, Vol. 48, No. 12, 2010, pp. 2739–2751. <https://doi.org/10.2514/1.43917>
- [24] Tamjani, A. Y., and Kapania, R. K., "Vibration of Plate with Curvilinear Stiffeners Using Mesh-Free Method," *AIAA Journal*, Vol. 48, No. 8, 2010, pp. 1569–1581. <https://doi.org/10.2514/1.43082>
- [25] Qin, X., Dong, C., Wang, F., and Qu, X., "Static and Dynamic Analyses of Isogeometric Curvilinearly Stiffened Plates," *Applied Mathematical Modelling*, Vol. 45, May 2017, pp. 336–364. <https://doi.org/10.1016/j.apm.2016.12.035>
- [26] Saeedi, A., Hassani, B., and Farzam, A., "Simultaneous Modeling and Structural Analysis of Curvilinearly Stiffened Plates Using an Isogeometric Approach," *Acta Mechanica*, Vol. 231, No. 8, 2020, pp. 3473–3498. <https://doi.org/10.1007/s00707-020-02725-4>
- [27] Hao, P., Wang, Y., Tang, H., Feng, S., and Wang, B., "A NURBS-Based Degenerated Stiffener Element for Isogeometric Static and Buckling Analysis," *Computer Methods in Applied Mechanics and Engineering*, Vol. 398, Aug. 2022, Paper 115245. <https://doi.org/10.1016/j.cma.2022.115245>
- [28] Jaunkis, N., Knight, N. F., Jr., and Ambur, D. R., "Formulation of an Improved Smeared Stiffener Theory for Buckling Analysis of Grid-Stiffened Composite Panels," *Composites, Part B: Engineering*, Vol. 27, No. 5, 1996, pp. 519–526. [https://doi.org/10.1016/1359-8368\(96\)00032-7](https://doi.org/10.1016/1359-8368(96)00032-7)
- [29] Wodesenbet, E., Kidane, S., and Pang, S.-S., "Optimization for Buckling Loads of Grid Stiffened Composite Panels," *Composite Structures*,

- Vol. 60, No. 2, 2003, pp. 159–169.  
[https://doi.org/10.1016/S0263-8223\(02\)00315-X](https://doi.org/10.1016/S0263-8223(02)00315-X)
- [30] Nemeth, M. P., “A Treatise on Equivalent-Plate Stiffnesses for Stiffened Laminated-Composite Plates and Plate-Like Lattices,” NASA TP-2011-216882, 2011, <https://ntrs.nasa.gov/citations/20110004039> [retrieved 18 May 2023].
- [31] Chen, J., Zhong, Y., Luo, Q., and Shi, Z., “Static and Dynamic Analysis of Isogrid Stiffened Composite Plates (ISCP) Using Equivalent Model Based on Variational Asymptotic Method,” *Thin-Walled Structures*, Vol. 163, June 2021, Paper 107671.  
<https://doi.org/10.1016/j.tws.2021.107671>
- [32] Wang, B., Tian, K., Hao, P., Zheng, Y., Ma, Y., and Wang, J., “Numerical-Based Smeared Stiffener Method for Global Buckling Analysis of Grid-Stiffened Composite Cylindrical Shells,” *Composite Structures*, Vol. 152, Sept. 2016, pp. 807–815.  
<https://doi.org/10.1016/j.compstruct.2016.05.096>
- [33] Liu, N., Yu, W., and Hodges, D. H., “Mechanics of Structure Genome-Based Global Buckling Analysis of Stiffened Composite Panels,” *Acta Mechanica*, Vol. 230, Nov. 2019, pp. 4109–4124.  
<https://doi.org/10.1007/s00070-018-2339-4>
- [34] Wang, D., and Abdalla, M. M., “Global and Local Buckling Analysis of Grid-Stiffened Composite Panels,” *Composite Structures*, Vol. 119, Jan. 2015, pp. 767–776.  
<https://doi.org/10.1016/j.compstruct.2014.09.050>
- [35] Wang, D., Abdalla, M. M., Wang, Z.-P., and Su, Z., “Streamline Stiffener Path Optimization (SSPO) for Embedded Stiffener Layout Design of Non-Uniform Curved Grid-Stiffened Composite (NCGC) Structures,” *Computer Methods in Applied Mechanics and Engineering*, Vol. 344, Feb. 2019, pp. 1021–1050.  
<https://doi.org/10.1016/j.cma.2018.09.013>
- [36] Mittelstedt, C., “Closed-Form Buckling Analysis of Stiffened Composite Plates and Identification of Minimum Stiffener Requirements,” *International Journal of Engineering Science*, Vol. 46, No. 10, 2008, pp. 1011–1034.  
<https://doi.org/10.1016/j.ijengsci.2008.02.004>
- [37] Stanford, B., Beran, P., and Bhatia, M., “Aeroelastic Topology Optimization of Blade-Stiffened Panels,” *Journal of Aircraft*, Vol. 51, No. 3, 2014, pp. 938–944.  
<https://doi.org/10.2514/1.C032500>
- [38] Townsend, S., and Kim, H. A., “A Level Set Topology Optimization Method for the Buckling of Shell Structures,” *Structural and Multidisciplinary Optimization*, Vol. 60, No. 5, 2019, pp. 1783–1800.  
<https://doi.org/10.1007/s00158-019-02374-9>
- [39] Zhao, W., and Kapania, R. K., “Prestressed Vibration of Stiffened Variable-Angle Tow Laminated Plates,” *AIAA Journal*, Vol. 57, No. 6, 2019, pp. 2575–2593.  
<https://doi.org/10.2514/1.J057719>
- [40] Oñate, E., *Structural Analysis with the Finite Element Method: Linear Statics, Vol. 2: Beams, Plates and Shells*, Springer Science and Business Media, Dordrecht, Netherland, 2013, pp. 58–62.  
<https://doi.org/10.1007/978-1-4020-8743-1>
- [41] Chen, C., Hon, Y., and Schaback, R., *Scientific Computing with Radial Basis Functions*, Dept. of Mathematics, Univ. of Southern Mississippi, Hattiesburg, MS, 2007, pp. 3–4, <http://num.math.uni-goettingen.de/schaback/SCwRBF.pdf> [retrieved 14 Oct. 2022].
- [42] Beckert, A., and Wendland, H., “Multivariate Interpolation for Fluid-Structure-Interaction Problems Using Radial Basis Functions,” *Aerospace Science and Technology*, Vol. 5, No. 2, 2001, pp. 125–134.  
[https://doi.org/10.1016/S1270-9638\(00\)01087-7](https://doi.org/10.1016/S1270-9638(00)01087-7)
- [43] Wendland, H., “Piecewise Polynomial, Positive Definite and Compactly Supported Radial Functions of Minimal Degree,” *Advances in Computational Mathematics*, Vol. 4, No. 1, 1995, pp. 389–396.  
<https://doi.org/10.1007/BF02123482>
- [44] Franke, R., “Scattered Data Interpolation: Tests of Some Methods,” *Mathematics of Computation*, Vol. 38, No. 157, 1982, pp. 181–200.  
<https://doi.org/10.2307/2007474>
- [45] Cheng, A.-D., Golberg, M., Kansa, E., and Zammito, G., “Exponential Convergence and  $H - c$  Multiquadric Collocation Method for Partial Differential Equations,” *Numerical Methods for Partial Differential Equations*, Vol. 19, No. 5, 2003, pp. 571–594.  
<https://doi.org/10.1002/num.10062>
- [46] Ferreira, A., “A Formulation of the Multiquadric Radial Basis Function Method for the Analysis of Laminated Composite Plates,” *Composite Structures*, Vol. 59, No. 3, 2003, pp. 385–392.  
[https://doi.org/10.1016/S0263-8223\(02\)00239-8](https://doi.org/10.1016/S0263-8223(02)00239-8)
- [47] Hardy, R. L., “Theory and Applications of the Multiquadric-Biharmonic Method 20 Years of Discovery 1968–1988,” *Computers & Mathematics with Applications*, Vol. 19, Nos. 8–9, 1990, pp. 163–208.  
[https://doi.org/10.1016/0898-1221\(90\)90272-L](https://doi.org/10.1016/0898-1221(90)90272-L)
- [48] Micchelli, C. A., “Interpolation of Scattered Data: Distance Matrices and Conditionally Positive Definite Functions,” *Approximation Theory and Spline Functions*, Springer, Berlin, 1984, pp. 143–145.  
[https://doi.org/10.1007/978-94-009-6466-2\\_7](https://doi.org/10.1007/978-94-009-6466-2_7)
- [49] Wang, S., and Wang, M. Y., “Radial Basis Functions and Level Set Method for Structural Topology Optimization,” *International Journal for Numerical Methods in Engineering*, Vol. 65, No. 12, 2006, pp. 2060–2090.  
<https://doi.org/10.1002/nme.1536>
- [50] Harder, R. L., and Desmarais, R. N., “Interpolation Using Surface Splines,” *Journal of Aircraft*, Vol. 9, No. 2, 1972, pp. 189–191.  
<https://doi.org/10.2514/3.44330>
- [51] Slemp, W. C., Bird, R. K., Kapania, R. K., Havens, D., Norris, A., and Olliffe, R., “Design, Optimization, and Evaluation of Integrally Stiffened Al-7050 Panel with Curved Stiffeners,” *Journal of Aircraft*, Vol. 48, No. 4, 2011, pp. 1163–1175.  
<https://doi.org/10.2514/1.C031118>
- [52] Hao, P., Wang, Y., Liu, C., Wang, B., Tian, K., Li, G., Wang, Q., and Jiang, L., “Hierarchical Nondeterministic Optimization of Curvilinearly Stiffened Panel with Multicutouts,” *AIAA Journal*, Vol. 56, No. 10, 2018, pp. 4180–4194.  
<https://doi.org/10.2514/1.J056856>
- [53] Gürdal, Z., and Olmedo, R., “In-Plane Response of Laminates with Spatially Varying Fiber Orientations: Variable Stiffness Concept,” *AIAA Journal*, Vol. 31, No. 4, 1993, pp. 751–758.  
<https://doi.org/10.2514/3.11613>
- [54] Alhajahmad, A., and Mittelstedt, C., “Buckling Performance of Curvilinear Grid-Stiffened Tow-Placed Composite Panels Considering Manufacturing Constraints,” *Composite Structures*, Vol. 260, March 2021, Paper 113271.  
<https://doi.org/10.1016/j.compstruct.2020.113271>

R. Ohayon  
*Associate Editor*